Quantifying climate change impacts on hydropower production under CMIP6 multi-model ensemble projections using SWAT model

Emrah Yalcin

Published online: 30 Aug 2023.

Submit your article to this journal ⬀

Article views: 214

View related articles ⬀

View Crossmark data ⬀

Quantifying climate change impacts on hydropower production under CMIP6 multi-model ensemble projections using SWAT model

Emrah Yalcin

Department of Civil Engineering, Kirsehir Ahi Evran University, Kirsehir, Turkey

ABSTRACT

This study assesses the effects of climate change on hydropower production in the most threatened highlands region of the Euphrates-Tigris Basin, with the case of the Dipni Project. This evaluation is based on the precipitation and temperature predictions of the multi-model ensembles produced by analysing the simulations of 24 global circulation models (GCMs) from the Coupled Model Intercomparison Project Phase 6 (CMIP6). The Soil and Water Assessment Tool (SWAT) model is utilized to estimate the future inflow rates of the Dipni reservoir under the Shared Socio-economic Pathway (SSP) scenarios of SSP245 and SSP585. The 25-year reservoir operations conducted in the past and three future periods indicate possible decreases of up to 10.1% and 21.5% in the annual energy production under the SSP245 and SSP585 scenarios, respectively. The results show the need to take adaptive measures against the projected impacts of climate change to achieve the targeted return for the coming decades.

1 Introduction

The threat of climate change is accelerating with the continuous emission of greenhouse gases and subsequent changes in the magnitude and seasonal variations of temperature and precipitation patterns in many parts of the globe (IPCC 2021). This acceleration heightens concerns about future water availability, particularly in regions where the water supply is currently dominated by melting snow (Stewart 2009, Hasson 2016, Nazeer *et al.* 2022). The climate change projections foresee an increasing trend in surface temperatures that will lead to significant changes in the seasonality of streamflow regimes of high-altitude basins in which snowmelt is the major runoff contributor (Barnett *et al.* 2005, Adam *et al.* 2009). In a warmer climate, less precipitation falls as snow in winter, and the melting of winter snow occurs earlier in spring. Thus, even without any changes in precipitation intensity, the peak runoff period shifts to winter and early spring, away from the months when the demand is highest (Barnett *et al.* 2005).

Dam construction is a long-standing strategy to supply water and hydroelectricity by regulating the temporal and spatial variations in the natural flow of rivers (Nilsson *et al.* 2005). The water-storage potential of a dam project is investigated generally using the historical streamflow records of representative stream-gauging stations located in or near the project catchment area, and all critical decisions on the project feasibility, optimum design of dam components, and determination of operational rules are taken based on these historical measurements. However, the system performance of dams, especially in mountainous areas, highly depends on the hydrological regime experiencing substantial alteration associated with changing climate (Duratorre *et al.* 2020, Wen *et al.* 2021, Qin *et al.* 2022, Xiang *et al.* 2022). Hence, it is

economically and technically crucial to assess the water supply and hydropower generation capabilities of dam projects, designed for an operational lifetime of at least 50 years, using the streamflow predictions attained under future climate conditions instead of past flow records (van Vliet *et al.* 2016, Ehsani *et al.* 2017, Turner *et al.* 2017).

The Euphrates-Tigris River Basin, shared among Turkey, Syria, Iraq, and Iran, is one of the most important transboundary basins in the world both politically and economically. The basin, hosting two important snow-fed rivers originating in Turkey, plays a critical role for the shared countries in not only hydropower generation but also water supply for irrigation and domestic use (Daggupati *et al.* 2017). While the riparian countries have been continuing their dam construction plans in relation to their own national interests without intercooperation for decades, the Eastern Mediterranean and Middle East region, covering the Euphrates-Tigris Basin wholly, has become a prominent climate change hotspot, warming almost two times more rapidly than the global mean (Giorgi 2006, Lelieveld *et al.* 2012, Zittis *et al.* 2022). Bozkurt and Sen (2013) assessed the effects of climate change in the Euphrates-Tigris Basin. Their results indicate that the northern highlands of the basin within the borders of Turkey are anticipated to experience more adverse direct effects of climate change compared to the territories of the other riparian countries, and a significant decline (by 26–57%) in the annual total surface runoff is expected for the river network lying in Turkey by the end of the present century. Özdoğan (2011) analysed the effects of projected climate change on the amount of water stored in snowpack in the mountains of the Euphrates-Tigris Basin. This study reports substantial decreases (between 10% and 60%) in the available snow

water, particularly later in the present century. Şen (2019) performed river flow projections up to the year 2050 for the upper portion of the Tigris Basin within the territories of Turkey. The results indicate a possible decrease by about 30% in the streamflow rates after 2040.

Despite the expected major changes in the future streamflow regime of the Euphrates-Tigris Basin, shown by these and several other studies (e.g. Nohara *et al.* 2006, Kitoh *et al.* 2008, Chenoweth *et al.* 2011), Turkey continues to increase the hydropower capacity on the Euphrates and Tigris Rivers and their tributaries through new dams and run-of-river type hydropower plants that are all designed without considering climate change impacts. Hence, the Turkish hydropower sector should assess the connection between water resources and energy generation under future climate conditions (Wasti *et al.* 2022). To the best of the knowledge, there is no study in the literature investigating the effects of potential climate change

scenarios upon the energy production of the planned or operating hydropower schemes within the Turkey portion covering the most threatened highlands region of the basin. There are similar gaps in the literature for the dams of the other riparian countries. This paper aims to address this gap by quantifying the impacts of projected climate change on the energy production capacity of the Dipni Dam and Hydroelectric Power Plant (HEPP) Project planned in the source region of the Tigris River (Fig. 1). Construction on the Dipni Project, whose feasibility was examined in 2008, has not started yet (EN-SU 2008).

For this purpose, simulations of daily precipitation, maximum temperature, and minimum temperature of 24 global circulation models (GCMs) from the latest published Coupled Model Intercomparison Project Phase 6 (CMIP6) are statistically downscaled using linear scaling and distribution mapping methods. By evaluating the best-performing GCMs and bias
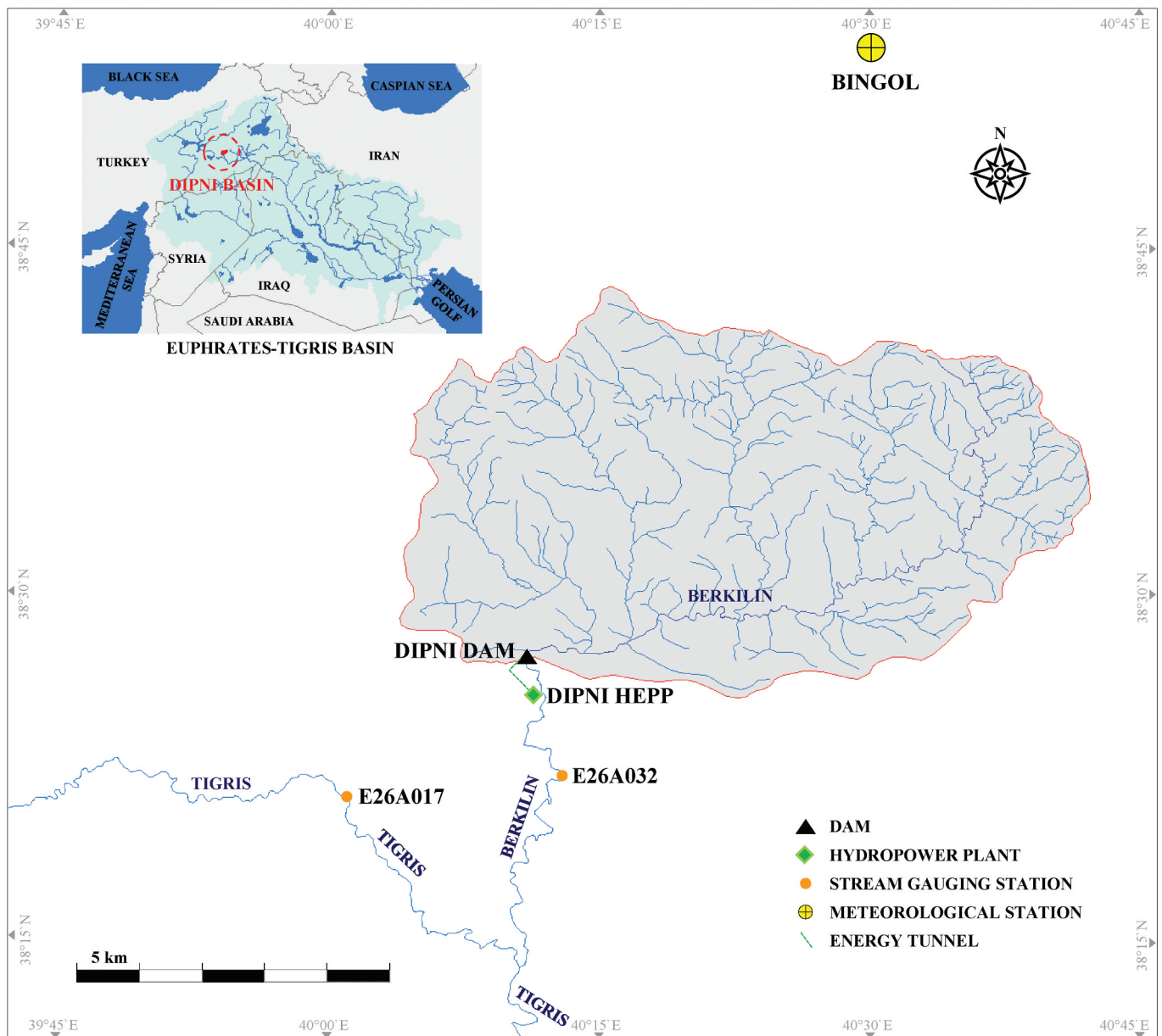

Figure 1. Map of the study area layout.

correction methods against the meteorological station records, multi-model ensemble mean predictions are produced for each climate variable under the CMIP6 historical experiment and the medium- and high-forcing Shared Socio-economic Pathway (SSP) scenarios SSP245 and SSP585 (O`Neill *et al.* 2016). Soil and Water Assessment Tool (SWAT) is preferred as the hydrological model to simulate streamflow under the historical and future climate scenarios due to its snow hydrology performance (Troin and Caya 2014). The SWAT model of the Dipni Basin, calibrated and validated against the historical streamflow records, is utilized to produce monthly inflow estimates for the Dipni reservoir for the future period of 2025–2099. Moreover, although lake evaporation does not constitute a major component of the reservoir water budget, the forthcoming changes in the monthly net evaporation rates are also taken into consideration to demonstrate the projected impacts of the warming climate on the basin. To make a realistic and fair comparison, a monthly reservoir operation algorithm is prepared based on the topographic and technical characteristics and reservoir operation policy specified in the project feasibility report (EN-SU 2008). The near-, mid-, and long-term potential impacts of climate change on the hydropower production of the Dipni Project are analysed in the 25-

year periods of 2025–2049, 2050–2074, and 2075–2099, respectively. A flowchart of the methodology applied in this study is depicted in Fig. 2.

2 Materials and methods

2.1 Overview of the study area

The Dipni Dam and HEPP Project is located within the borders of Diyarbakir province in the Southeastern Anatolia Region of Turkey, as presented in Fig. 1. The Dipni Project is planned with a total reservoir volume of 949 hm³ at elevations of 850 to 715 m of Berkilin Creek, between latitudes 38°25' and 38°31'N and longitudes 40°10' and 40°29'E (EN-SU 2008). Berkilin Creek is one of the upstream branches of the Tigris River, the second-longest river in western Asia (after the Euphrates). There is no other water resource scheme located upstream of the Dipni Project, and the Dicle Dam reservoir, with a maximum water level of 710 m, lies just downstream of the Dipni power plant (Yalcin and Tigrek 2019). The dam is designed to be a roller-compacted concrete type 107 m in height from the thalweg elevation of 746 m. The maximum and minimum water levels of the Dipni reservoir are 850 m
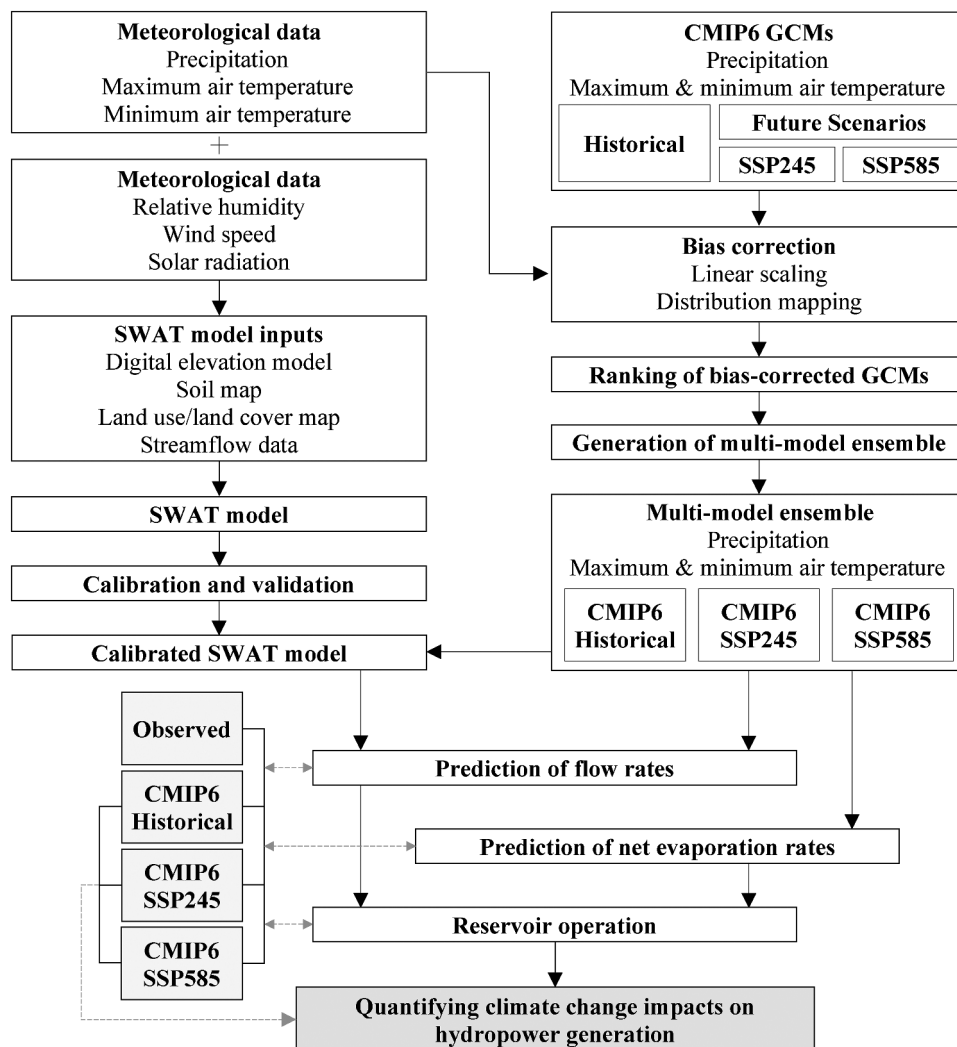

Figure 2. Flowchart of the applied methodology.

and 820 m, respectively. The spillway capacity of the dam is designated to be 4093 m³/s. The plan is to transfer the water stored in the Dipni reservoir (with an active storage capacity of 740 hm³) to the power plant through a circular energy tunnel 4 m in diameter and 4600 m in length with a 0.001 m/m bed slope, and a penstock 3.6 m in diameter and 150 m in length. The tail water level of the power plant is considered to be 715 m. The power plant is optimized for a design discharge of 25 m³/s with two units of Francis-type turbines that corresponds to a total installed power capacity of 29 MW (EN-SU 2008).

Berkilin Creek drains an area of 1275 km² along the 76 km flow route from its source to the Dipni Dam location, as illustrated in Fig. 1. The flows of Berkilin Creek were measured at the Cayustu stream-gauging station (SGS) (Station ID: E26A032), located at an altitude 57 m downstream from the Dipni Dam axis, for the period from October 1988 to September 1997 (Fig. 1). The Cayustu SGS, operated by the General Directorate of Electrical Power Resources Survey and Development Administration (EIE), has a drainage area of 1503.6 km², and its nine years of flow data, with a mean value of 28.2 m³/s, is not a long enough period to calibrate and validate the hydrological model that will be generated (DSI 2022). Therefore, the flow measurements of the Cayonu SGS (Station ID: E26A017) located on the Tigris River, approximately 28 km upstream of the conjunction of the Tigris River and Berkilin Creek, are utilized to provide a longer historical flow dataset for use in the hydrological modelling and reservoir operation studies (Fig. 1). The Cayonu SGS, also operated by EIE, drains an area of 1186 km² and has uninterrupted flow measurements with a mean value of 24.3 m³/s in the period from October 1971 to September 1997 (DSI 2022). Using the relationship between the monthly mean flow measurements of the Cayustu and Cayonu stations, producing a high Pearson's correlation value of 0.96, a 25-year representative monthly flow dataset for the 1972–1996 period is determined for the Cayustu station, with a mean flow rate of 31.1 m³/s. The extended runoff rates of the Cayustu station are brought to the dam location using the catchment area ratio between the Cayustu station and Dipni Dam. Accordingly, the mean historical flow rate at the Dipni Dam location is computed as 26.3 m³/s.

In this study, all climate analyses of the Dipni Basin, having an average altitude of 1283 m, are based on the measurements of the Bingol meteorological station (MS) (Station ID: 17203), operated by the Turkish State Meteorological Service (MGM) at an altitude of 1139 m (Fig. 1). Although the project is within the borders of Diyarbakir province, the climatic characteristics of the Dipni Basin differ from the measurements at the Diyarbakir MS (Station ID: 17280) located at 674 m elevation. The main portion of the Dipni Basin is at the foot of the Southeast Taurus Mountain Range, which blocks cold winds from the north, and the basin is less affected by the desert climate in the south compared to Diyarbakir province (FPGA 1968). There are other stations inside or near the studied basin (e.g. Aricak, Hani, Lice, and Yayla); however, the Bingol MS is the only representative station that has the long-term precipitation, maximum and minimum temperature, wind speed, relative humidity, and solar radiation measurements required

to constitute the hydrological model for the extended historical flow period (MGM 2022b). According to the Bingol MS records in the 1961–2021 observation period, the annual average temperature is 12.2°C, the annual total precipitation average is 943.6 mm, the annual average number of snow-covered days is 72.5, and the monthly average snow depths are between 6.6 and 38.5 cm. The snow cover, which can reach up to 2 m thick, starts to decrease from mid-March onwards due to a rise in temperature (MGM 2022c).

2.2 Selection of the multi-model ensembles of CMIP6 GCMs

Daily precipitation, maximum temperature, and minimum temperature datasets simulated by 24 CMIP6 GCMs as part of the CMIP6 historical experiment and future emission scenarios of SSP245 and SSP585 are retrieved from the Earth System Grid Federation (ESGF) website (ESGF 2022). The past data covers the period 1961–2014, and the future data includes the years 2025–2099. In order to provide consistency and perform a fair comparison of the GCMs' performances, the GCM selection is based on the time scale (daily) and availability of the considered SSP scenarios under the first ensemble member with a variant label of r1i1p1f1 (i.e. realization [r1], initialization [i1], physics [p1], and forcing [f1] indices) (Bağçaci *et al.* 2021, Sun *et al.* 2022). The model IDs, modelling centres, and spatial resolutions of the selected GCMs are detailed in Table 1. The climate datasets, downloaded from the ESGF database in NetCDF file format, with different grid sizes are resampled into a regular 0.5° × 0.5° longitude and latitude mesh for the border coordinates of Turkey using the first-order conservative remapping method (Jones 1999), to have a common spatial resolution for facilitating fair comparisons. The open-source Climate Data Operators (CDO) software developed and provided by the Max Planck Institute for Meteorology (Schulzweida 2021) is utilized within the Cygwin terminal (Cygwin 2022) for all merging, manipulating, interpolating, and spatial clipping processes applied to the CMIP6 model datasets.

Bias correction is essential to adjust GCM predictions against possible systematic errors to match certain observed climate characteristics (e.g. distribution, sequencing, and magnitude) prior to utilization in hydrological modelling studies (Tan *et al.* 2020). In this study, two statistical downscaling methods, namely linear scaling and distribution mapping, are employed separately to perform bias correction of the GCM outputs for the location of the Bingol MS with respect to the daily measured data of the 1961–2014 period (MGM 2022b). For this process, the open-source Climate Model Data for Hydrologic Modelling (CMhyd) tool (Rathjens *et al.* 2016) is utilized to reduce statistical biases in the daily precipitation and temperature outputs of the analysed CMIP6 GCMs at the point scale. Hence, while analysing the reliability of the bias-corrected GCM outputs, it will also be possible to evaluate the regionally dependent skills of linear scaling and distribution mapping methods for the studied area (Chen *et al.* 2013).

The performances of the bias-corrected historical simulations of the 24 CMIP6 GCMs are evaluated on a monthly basis in the 1961–2014 period using four performance measures,

Table 1. Description of the CMIP6 GCMs considered in this study.

Model ID	Institution	Horizontal resolution (longitude × latitude)	References
ACCESS-CM2	Commonwealth Scientific and Industrial Research Organization (CSIRO), Australia Australian Research Council Centre of Excellence for Climate System Science (ARCCSS), Australia	1.875° × 1.25°	Dix *et al*. (2019a, 2019b)
ACCESS-ESM1-5	Commonwealth Scientific and Industrial Research Organization (CSIRO), Australia	1.875° × 1.25°	Ziehn *et al*. (2019a, 2019b)
BCC-CSM2-MR	Beijing Climate Center (BCC), China	1.125° × (1.112–1.121)°	Wu *et al*. (2018), Xin *et al*. (2019)
CanESM5	Canadian Centre for Climate Modelling and Analysis (CCCma), Canada	2.8125° × (2.767–2.791)°	Swart *et al*. (2019a, 2019b)
CMCC-ESM2	Centro Euro-Mediterraneo sui Cambiamenti Climatici (CMCC), Italy	1.25° × 0.9424084°	Lovato *et al*. (2021a, 2021b)
EC-Earth3	EC – Earth Consortium, Europe	0.703125° × (0.696–0.702)°	EC-Earth (2019a, 2019b)
EC-Earth3-CC	EC– Earth Consortium, Europe	0.703125° × (0.696–0.702)°	EC-Earth (2021a, 2021b)
EC-Earth3-Veg	EC – Earth Consortium, Europe	0.703125° × (0.696–0.702)°	EC-Earth (2019c, 2019d)
EC-Earth3-Veg-LR	EC – Earth Consortium, Europe	1.125° × (1.112–1.121)°	EC-Earth (2020a, 2020b)
FGOALS-g3	Chinese Academy of Sciences (CAS), China	2° × (2.025–5.181)°	Li (2019a, 2019b)
GFDL-CM4	National Oceanic and Atmospheric Administration – Geophysical Fluid Dynamics Laboratory (NOAA-GFDL), USA	1.25° × 1°	Guo *et al*. (2018a, 2018b)
GFDL-ESM4	National Oceanic and Atmospheric Administration – Geophysical Fluid Dynamics Laboratory (NOAA-GFDL), USA	1.25° × 1°	John *et al*. (2018), Krasting *et al*. (2018)
INM-CM4-8	Institute for Numerical Mathematics (INM), Russia	2° × 1.5°	Volodin *et al*. (2019a, 2019b)
INM-CM5-0	Institute for Numerical Mathematics (INM), Russia	2° × 1.5°	Volodin *et al*. (2019c, 2019d)
IPSL-CM6A-LR	Institut Pierre Simon Laplace (IPSL), France	2.5° × 1.267606°	Boucher *et al*. (2018, 2019)
KIOST-ESM	Korea Institute of Ocean Science and Technology (KIOST), Korea	*for precipitation datasets* 1.875° × 1.875° *for temperature datasets* 1.875° × 1.894737°	Kim *et al*. (2019a, 2019b)
MIROC6	Japan Agency for Marine-Earth Science and Technology (JAMSTEC), Japan Atmosphere and Ocean Research Institute – The University of Tokyo (AORI), Japan National Institute for Environmental Studies (NIES), Japan RIKEN Center for Computational Science (R-CCS), Japan	1.40625° × (1.389–1.401)°	Tatebe and Watanabe (2018), Shiogama *et al*. (2019)
MPI-ESM1-2-HR	Max Planck Institute for Meteorology (MPI-M), Germany Deutsches Klimarechenzentrum (DKRZ), Germany	0.9375° × (0.927–0.935)°	Jungclaus *et al*. (2019), Schupfner *et al*. (2019)
MPI-ESM1-2-LR	Max Planck Institute for Meteorology (MPI-M), Germany	1.875° × (1.850–1.865)°	Wieners *et al*. (2019a, 2019b)
MRI-ESM2-0	Meteorological Research Institute (MRI), Japan	1.125° × (1.112–1.121)°	Yukimoto *et al*. (2019a, 2019b)
NESM3	Nanjing University of Information Science and Technology (NUIST), China	1.875° × (1.850–1.865)°	Cao (2019), Cao and Wang (2019)
NorESM2-LM	NorESM Climate Modeling Consortium, Norway	2.5° × 1.894737°	Seland *et al*. (2019a, 2019b)
NorESM2-MM	NorESM Climate Modeling Consortium, Norway	1.25° × 0.9424084°	Bentsen *et al*. (2019a, 2019b)
TaiESM1	Research Center for Environmental Changes – Academia Sinica (AS-RCEC), Taiwan	1.25° × 0.9424084°	Lee and Liang (2020a, 2020b)

namely the modified index of agreement (*md*) (Legates and McCabe 1999), normalized root mean square error (nRMSE) (Almeida *et al*. 2015), Kling-Gupta efficiency metric (KGE) (Gupta *et al*. 2009), and fractions skill score (FSS) (Roberts and Lean 2008). According to the calculated performance metrics for the bias-corrected monthly total precipitation, monthly mean maximum temperature, and monthly mean minimum temperature rates, the GCMs are ranked from best to worst based on each performance measure for each climate variable separately. Then, a comprehensive rating metric (RM) (Chen *et al*. 2011) is utilized to rank the GCMs in descending order according to their performance for each climate variable by considering all four performance measures. While the rankings determined for the GCMs for the precipitation variable are directly used in deriving a multi-model ensemble mean for precipitation predictions, the comprehensive RM values of the GCMs obtained for the maximum and minimum temperature variables are combined to derive the overall ranking of the GCMs for temperature predictions. Thus, two individual GCM rankings for precipitation and temperature predictions are obtained for each considered bias correction method.

The review of the literature reveals that using only one GCM is not appropriate to assess the uncertainties associated with the future climate (Weigel *et al*. 2010, Miao *et al*. 2012, Kim *et al*. 2016). Therefore, to reduce the uncertainties arising from GCM structure, assumptions, approximations, initial conditions, and parametrization, the use of a small ensemble of 3 to 10 better-performing GCMs is preferred to using the single best-performing one (Kim *et al*. 2016, Ahmed *et al*. 2019). Although there is no consensus on the selection of the optimum number of GCMs to generate a multi-model ensemble, in this study, the ensembles of the top four GCMs are considered according to the GCM rankings obtained for precipitation and temperature predictions separately (Ahmed *et al*. 2019, Bağçaci *et al*. 2021). The mean daily time series of multi-model ensembles for the CMIP6 historical experiment and future scenarios of SSP245 and SSP585 are calculated according to the simple mean technique by just averaging the daily bias-corrected simulations of the four top-ranked GCMs for each climate variable (Ahmed *et al*. 2019). The use of multi-model ensembles instead of one GCM is validated by comparing the monthly-based performance metrics of the multi-model ensemble means and individual GCMs for each climate variable. Finally, by comparing the performance measures of the multi-model ensemble means observed using the linear scaling and distribution mapping methods for each climate variable, the best-performing multi-model ensembles are determined for use in the SWAT model analyses. For convenience, in the rest of the text, the multi-model ensemble mean predictions for the location of the

Bingol MS are referred to as "CMIP6 historical" for the historical 1972–1996 period and "CMIP6 SSP245" and "CMIP6 SSP585" for the future 2025–2099 period.

2.3 Construction of SWAT model

SWAT is a physically based semi-distributed river basin model developed by the United States Department of Agriculture – Agricultural Research Service (USDA-ARS) (Neitsch *et al.* 2011, Arnold *et al.* 2013). In this study, the SWAT model of the Dipni Basin is constructed within ArcSWAT 2012 (revision 664) using three main types of physiographic data, namely a digital elevation model (DEM), land use/land cover (LULC)

map, and soil map, as presented in Fig. 3. The global coverage public domain database of the Shuttle Radar Topography Mission (SRTM) is used to obtain void-filled digital terrain elevation data at a resolution of 1 arc-second (i.e. approximately 30 m) (USGS 2014). The dominant land cover types in the basin are extracted in grid format from the Global Land Cover 2000 (GLC2000) version 2.0 dataset at 1 km spatial resolution (EC-JRC 2006). The grid-based watershed soil characteristics are derived from the Digital Soil Map of the World (DSMW) version 3.6 at a scale of 1:5 million (FAO 2007).

The daily climatic variables required by SWAT to simulate hydrological processes on a monthly basis are precipitation (mm), maximum and minimum air temperature (°C), solar
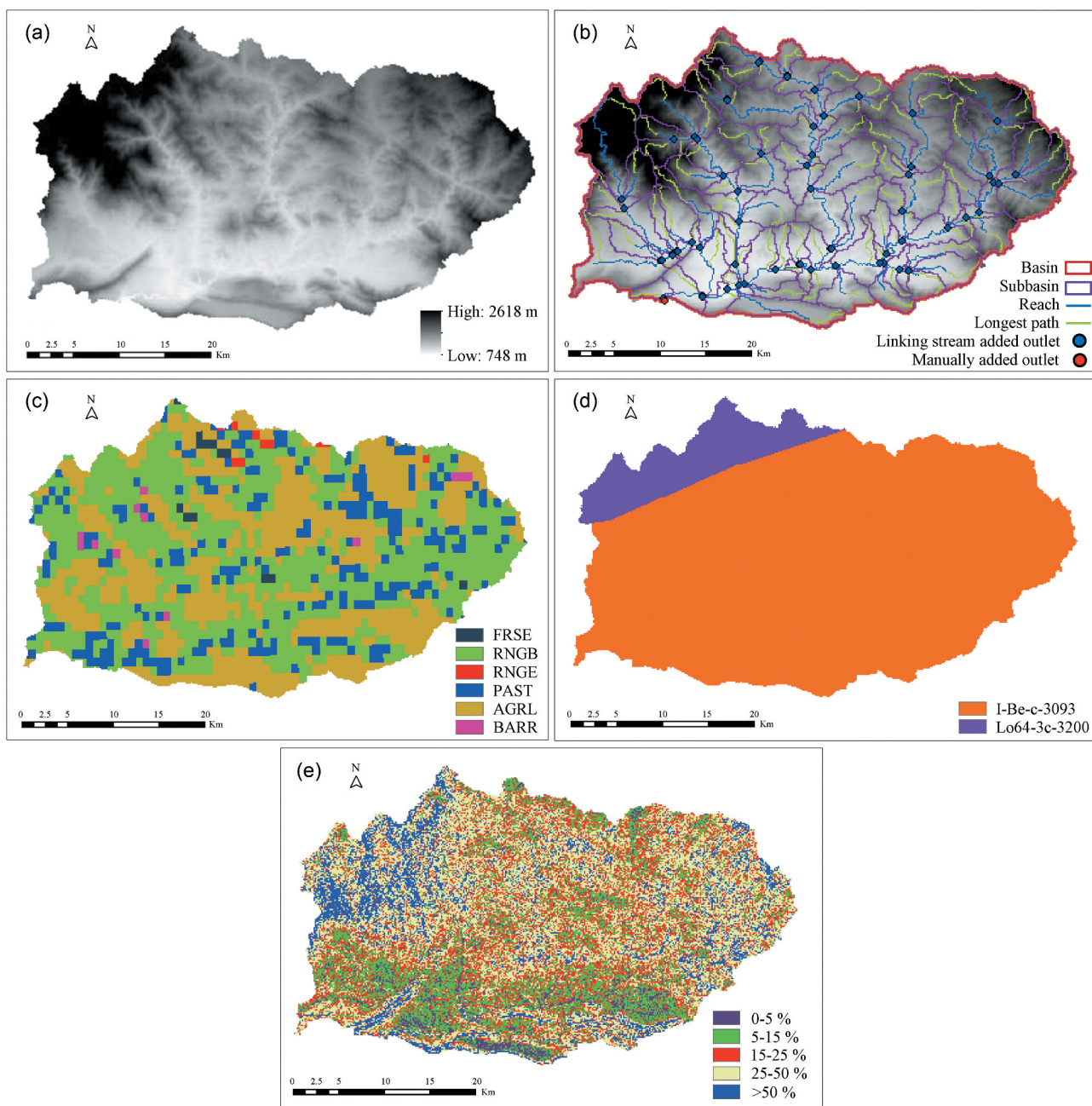

Figure 3. Steps of the SWAT model setup: (a) DEM, (b) watershed delineation, (c) land cover classes, (d) soil types, and (e) slope classes.

radiation (MJ/m²), wind speed (m/s), and relative humidity. In order to simulate the monthly inflow rates of the Dipni reservoir in the mentioned extended historical flow period of 1972–1996, the daily weather records of the Bingol station for the analysis period from 1 January 1968 to 31 December 1996, including four years of model warm-up period (i.e. 1968–1971), are inputted into the model together with the monthly weather statistics and geographic position information (in terms of latitude, longitude, and elevation) of the station (MGM 2022b).

The weather generator within SWAT uses the monthly weather statistics to generate representative daily values for missing variables or to fill gaps in the measured data. These statistics are of great importance in simulating flow rates based on only the precipitation and temperature variables of the CMIP6 historical experiment and future scenarios of SSP245 and SSP585 in the absence of solar radiation, wind speed, and relative humidity data. Hence, in order to catch long-term trends not reflecting short-term fluctuations, the monthly statistical parameters of the Bingol MS are determined for the entire measurement period (i.e. 1961–2021). All monthly weather statistics, except the ones for half-hour rainfall and dew point temperature, are calculated with the WGNmaker4.1.xlsm Microsoft Excel macro (Boisrame 2011). The monthly maximum half-hour rainfall rates of the Bingol MS are computed by multiplying the monthly maximum daily precipitation records with the half-hour pluviograph coefficient of the station (MGM 2022a). The monthly average daily dew point temperatures are calculated with the DOS-based dew02.exe program (Liersch 2003) using the daily maximum and minimum temperature and daily percent relative humidity measurements of the station.

The last step of the model construction is generating elevation bands for the sub-basins to account for orographic effects on both precipitation and temperature in each sub-basin and, hence, to model snowpack and snowmelt processes separately for each individual elevation band (Arnold et al. 2013). In this context, using the DOS-based stand-alone Make_ELEV_BAND program (Abbaspour 2015a), five elevation bands are defined for all sub-basins, except where the maximum relief is too small to take into account changes in precipitation and temperature due to altitude.

2.4 SWAT model calibration and streamflow predictions

Before analysing the possible impacts of climate change on the inflow rates of the Dipni Dam, the developed SWAT model is calibrated and validated against the 25-year monthly runoff time series of the extended historical flow period using the measured climate data. The first 17 years of the 1972–1996 period are considered the calibration period, and the flow data for the remaining eight years are utilized to verify the calibrated model. The sensitivity, calibration, validation, and uncertainty analyses are conducted within the public domain SWAT Calibration and Uncertainty Procedures (SWAT-CUP) software package (Abbaspour 2015a) using the Sequential Uncertainty Fitting Version 2 (SUFI-2) algorithm (Abbaspour et al. 2004, 2007) as the optimization procedure. In the SUFI-2 algorithm, all uncertainties arising from input

data, modelling parameters, and conceptual model are mapped onto the parameter ranges in an iterative process, and model output uncertainty is quantified by the 95% prediction uncertainty (95PPU) in terms of P factor and R factor. While the P factor is the fraction of the observed flow data captured within the 95PPU band, the R factor, denoting the degree of uncertainty, is the ratio of the average width of the 95PPU band to the standard deviation of the observed flows. Due to a trade-off between these two indices, a larger P factor can only be achieved with a larger R factor. In order to establish a balance between these two indices, SUFI-2 should be iterated a few times, starting with wide parameter ranges and then narrowing these ranges at each iteration in accordance with the objective function value until an optimum set of parameter ranges is obtained (Abbaspour et al. 2015b). In this study, Nash-Sutcliffe Efficiency (NSE) (Nash and Sutcliffe 1970) is preferred as the objective function of the SUFI-2 algorithm.

Model calibration is conducted in three stages to avoid parameter interaction and identifiability problems. In the first stage, the precipitation (PLAPS) and temperature (TLAPS) lapse rate parameters are calibrated and fixed to their best simulation values. Secondly, the same procedure is applied for the sensitive snow-related parameters. At last, other sensitive parameters related to groundwater, soil, hydrological response unit, management, and main channel are calibrated under the pre-fixed values of the location-specific parameters. At each phase of the calibration process, the sensitivity of each parameter is analysed separately through a single iteration with 50 simulations, and then a combined iteration composed of 500 simulations is performed for the sensitive parameters and their initial ranges identified in these one-at-a-time analyses. These combined iterations are repeated until acceptable P factor, R factor, and NSE values are reached. Accordingly, the parameter ranges of the final iteration are taken as the calibrated parameter ranges, and the parameter set providing the best simulation (i.e. the simulation with the highest NSE value against the inputted historical flow data) of the final iteration is referred to as the best-performing parameter values. After accomplishing the model calibration process for the 1972–1988 period, the calibrated parameter ranges are validated against the monthly mean inflow rates of the Dipni reservoir for the period from 1989 to 1996 by executing a single combined iteration of 500 simulations using the calibrated parameter ranges. More detailed information on the applied calibration procedure can be found in Abbaspour et al. (2004, 2007, 2015b) and Yalcin (2019).

The best simulation results attained in the model calibration and validation stages belong to the simulation with the highest objective function value against the inputted historical flow data. Hence, it is not realistic to take into account the best simulation results to evaluate whether the flow forecasting performance of the SWAT model is adequate in the absence of flow records. Therefore, in order to assess the flow prediction performance of the calibrated SWAT model, two flow forecasting approaches, namely best simulation estimates and 50% uncertainty level median values of the 95PPU band (M95PPU), are considered (Lemann et al. 2017, Farsani et al. 2019, Yalcin 2019). While best simulation estimates are

obtained with a single run using the best-performing parameter set of the calibration period, M95PPU values are attained with a single combined iteration using the calibrated parameter ranges. The usability of these approaches is evaluated for the validation period in terms of the statistics br^2, NSE, percent bias (PBIAS), and RSR. br^2 is defined as the coefficient of determination (r^2) multiplied by the slope of the linear regression line (b) forcing the intercept through zero, and RSR equals the ratio of the root mean square error to the standard deviation of the observed data.

After verification of these two flow forecasting approaches for the validation period, the calibrated SWAT model is simulated for the years 1972 to 1996 to attain the monthly best simulation estimates and M95PPU values for the whole extended historical flow period. Then, the calibrated model simulations are re-performed in 25-year periods using the precipitation and temperature predictions of CMIP6 historical and the future scenarios of CMIP6 SSP245 and CMIP6 SSP585 to obtain the monthly mean inflow estimates of the Dipni reservoir under both flow forecasting approaches for the historical 1972–1996 period and the near-, mid-, and far-future periods of 2025–2049, 2050–2074, and 2075–2099, respectively.

2.5 Lake evaporation under changing climate conditions

The monthly net evaporation rates of the Dipni reservoir are calculated based on the correlation relationship between the long-term (i.e. the 1961–2021 period) mean monthly total evaporation and temperature records of the Bingol MS (MGM 2022c). To make a consistent comparison between the evaporation rates calculated using the station records and multi-model ensemble mean predictions, the average of the maximum and minimum temperature values is considered as the mean temperature (Usul 2009). Assuming a 0.5°C decrease in temperature per 100 m increase in altitude, the mean monthly temperature records observed at the Bingol MS in the 1972–1996 period are transformed into the maximum water level of the Dipni reservoir. Then, the monthly total evaporation quantities corresponding to these transformed temperatures are calculated according to the correlation between the temperature and evaporation records of the Bingol station. Next, the computed evaporation values are multiplied by the pan coefficient (0.7) to convert the pan evaporation values into actual evaporation rates from the lake surface (Usul 2009). Finally, the monthly net evaporation rates per unit area are determined by subtracting the mean monthly precipitation records of the Bingol station in the 1972–1996 period from the calculated actual evaporation rates. This procedure, applied to the observation-based historical lake evaporation values, is repeated seven times, using the precipitation and temperature predictions of CMIP6 historical and the future scenarios of CMIP6 SSP245 and CMIP6 SSP585 to calculate monthly net evaporation rates for the historical and near-, mid-, and far-future periods, respectively.

2.6 Reservoir operation scheme

An operation algorithm is written in Visual Basic for Applications in Excel software to conduct the reservoir operations. The operation studies are performed on a monthly basis in accordance with a reservoir operation policy that guarantees maximum firm power in 95% of the operation period and maximizes secondary power unrestricted up to the installed capacity (EN-SU 2008). The topographical and technical features of the Dipni Project (EN-SU 2008) together with the monthly environmental water supplies, referred to as non-power releases, are the fixed inputs of the operation algorithm. The topographical features are described through the use of volume–area and elevation curves. The technical data include the maximum and minimum operation levels, tailwater level, design discharge, penstock and energy tunnel characteristics (number, diameter, and length), number and type of turbines, turbine efficiency curve, and spillway capacity. The monthly mean inflow values and mean monthly evaporation rates from the reservoir water surface are the changing input datasets of the reservoir operations repeated for each of the analysed climate conditions over the 25-year historical and future time periods. The monthly environmental water requirements for the continuity of the natural ecosystem due to the energy tunnel structure involved in the project are accepted as 10% of the historical mean monthly flow rates on the Dipni Dam axis in the last 10 years (i.e. 1987–1996) of the SGS measurements (Yalcin and Tigrek 2019).

For all reservoir operations, the initial reservoir storage is set to be equal to the total reservoir capacity, and for the ending storage, the algorithm is constrained to turbine all available water in the active storage in line with the power plant capacity. Accordingly, the operation studies are performed 11 times using the observed and estimated (both M9599U values and best simulation estimates) inflow datasets under the historical and future climate conditions to assess climate change impacts not only on the firm and secondary energy productions of the Dipni HEPP but also on the spillway releases, firm discharge, and regulation ratio of the project.

3 Results and discussion

3.1 Accuracy analysis of the CMIP6 multi-model ensemble mean predictions

In the present study, four statistical performance metrics – md, nRMSE, KGE, and FSS – are used to assess the accuracy of the bias-corrected monthly time series of the precipitation, maximum temperature, and minimum temperature variables simulated by the 24 GCMs under the CMIP6 historical experiment in replicating the mean and variability of the observed records of the Bingol MS for the 1961–2014 period. Tables 2 and 3 show the performance metrics for each GCM in simulating the precipitation and temperature variables after applying bias correction with linear scaling and distribution mapping, respectively. While values closest to 1 indicate the best GCM performance for the statistics of md, KGE, and FSS, the GCM with an nRMSE value nearest to 0 has the best performance in terms of nRMSE for the considered climate variable. The ranks attained by the GCMs corresponding to these four metrics are used to calculate the RM values of each GCM for each climate variable. The RM values of the GCMs obtained for the maximum and minimum temperature variables are combined to derive the overall ranking of the GCMs for temperature

Table 2. Performance metrics and the rankings of GCMs after bias correction with linear scaling.

CMIP6 GCMs	Precipitation					Minimum temperature					Maximum temperature					Temperature
	md	nRMSE	KGE	FSS	RM (rank)	md	nRMSE	KGE	FSS	RM	md	nRMSE	KGE	FSS	RM	RM (rank)
ACCESS-CM2	0.603	0.152	0.513	0.770	0.500 (13)	0.872	0.083	0.957	0.988	0.042	0.852	0.089	0.935	0.958	0.010	0.021 (24)
ACCESS-ESM1-5	0.596	0.151	0.520	0.773	0.521 (12)	0.886	0.072	0.967	0.991	0.396	0.873	0.072	0.953	0.973	0.677	0.542 (9)
BCC-CSM2-MR	0.603	0.149	0.513	0.776	0.583 (10)	0.884	0.075	0.965	0.990	0.260	0.858	0.079	0.948	0.966	0.250	0.250 (19)
CanESM5	0.612	0.142	0.535	0.794	0.854 (3)	0.888	0.071	0.969	0.991	0.500	0.874	0.074	0.951	0.971	0.583	0.521 (11)
CMCC-ESM2	0.615	0.145	0.529	0.786	0.813 (5)	0.893	0.070	0.970	0.991	0.729	0.874	0.075	0.952	0.971	0.604	0.667 (6)
EC-Earth3	0.587	0.163	0.496	0.752	0.24 (18)	0.882	0.077	0.964	0.990	0.188	0.859	0.081	0.941	0.965	0.177	0.188 (22)
EC-Earth3-CC	0.587	0.154	0.523	0.768	0.448 (14)	0.886	0.074	0.966	0.990	0.313	0.863	0.077	0.950	0.968	0.375	0.313 (16)
EC-Earth3-Veg	0.576	0.160	0.494	0.754	0.229 (19)	0.882	0.076	0.962	0.990	0.188	0.865	0.078	0.938	0.968	0.271	0.229 (21)
EC-Earth3-Veg-LR	0.575	0.165	0.470	0.741	0.125 (21)	0.876	0.082	0.959	0.988	0.083	0.853	0.086	0.938	0.961	0.063	0.063 (23)
FGOALS-g3	0.605	0.147	0.510	0.778	0.615 (8)	0.887	0.071	0.964	0.991	0.427	0.859	0.081	0.931	0.965	0.115	0.292 (18)
GFDL-CM4	0.631	0.136	0.566	0.810	0.958 (1)	0.898	0.064	0.974	0.993	0.958	0.874	0.073	0.957	0.972	0.677	0.813 (5)
GFDL-ESM4	0.609	0.145	0.518	0.783	0.719 (6)	0.896	0.067	0.972	0.992	0.906	0.877	0.071	0.957	0.973	0.833	0.875 (2)
INM-CM4-8	0.595	0.152	0.510	0.765	0.385 (15)	0.895	0.067	0.970	0.992	0.854	0.879	0.071	0.958	0.973	0.875	0.875 (3)
INM-CM5-0	0.608	0.150	0.525	0.774	0.635 (7)	0.893	0.068	0.971	0.992	0.833	0.879	0.070	0.960	0.974	0.917	0.896 (1)
IPSL-CM6A-LR	0.614	0.144	0.539	0.789	0.844 (4)	0.892	0.068	0.971	0.992	0.792	0.855	0.085	0.941	0.962	0.104	0.438 (14)
KIOST-ESM	0.576	0.152	0.496	0.765	0.323 (17)	0.858	0.091	0.947	0.985	0.000	0.864	0.076	0.952	0.969	0.458	0.250 (20)
MIROC6	0.600	0.149	0.511	0.777	0.531 (11)	0.882	0.079	0.961	0.989	0.125	0.879	0.071	0.955	0.973	0.792	0.458 (13)
MPI-ESM1-2-HR	0.572	0.170	0.450	0.726	0.063 (22)	0.890	0.070	0.969	0.991	0.656	0.868	0.077	0.946	0.969	0.417	0.542 (10)
MPI-ESM1-2-LR	0.602	0.156	0.491	0.758	0.333 (16)	0.888	0.070	0.969	0.991	0.604	0.872	0.072	0.950	0.973	0.604	0.604 (8)
MRI-ESM2-0	0.601	0.147	0.513	0.777	0.604 (9)	0.891	0.071	0.967	0.991	0.573	0.874	0.072	0.958	0.973	0.708	0.667 (7)
NESM3	0.560	0.172	0.441	0.721	0.021 (24)	0.888	0.070	0.966	0.991	0.542	0.865	0.076	0.946	0.969	0.427	0.500 (12)
NorESM2-LM	0.556	0.163	0.435	0.734	0.052 (23)	0.890	0.069	0.971	0.992	0.740	0.876	0.068	0.962	0.975	0.917	0.833 (4)
NorESM2-MM	0.580	0.157	0.467	0.749	0.198 (20)	0.887	0.073	0.967	0.991	0.365	0.865	0.077	0.951	0.968	0.396	0.354 (15)
TaiESM1	0.621	0.143	0.566	0.795	0.906 (2)	0.887	0.072	0.968	0.991	0.427	0.862	0.080	0.946	0.966	0.250	0.313 (17)

Table 3. Performance metrics and the rankings of GCMs after bias correction with distribution mapping.

CMIP6 GCMs	Precipitation					Minimum temperature					Maximum temperature					Temperature
	md	nRMSE	KGE	FSS	RM (rank)	md	nRMSE	KGE	FSS	RM	md	nRMSE	KGE	FSS	RM	RM (rank)
ACCESS-CM2	0.579	0.169	0.458	0.730	0.615 (7)	0.880	0.078	0.961	0.989	0.000	0.864	0.081	0.947	0.965	0.031	0.000 (24)
ACCESS-ESM1-5	0.571	0.168	0.465	0.733	0.635 (6)	0.883	0.074	0.965	0.990	0.208	0.870	0.076	0.949	0.970	0.156	0.125 (21)
BCC-CSM2-MR	0.570	0.169	0.451	0.727	0.427 (14)	0.892	0.070	0.969	0.991	0.802	0.872	0.072	0.957	0.973	0.604	0.792 (4)
CanESM5	0.568	0.175	0.439	0.719	0.240 (20)	0.884	0.074	0.966	0.990	0.219	0.875	0.073	0.952	0.972	0.500	0.354 (16)
CMCC-ESM2	0.588	0.158	0.487	0.752	0.885 (3)	0.896	0.069	0.970	0.992	0.938	0.877	0.073	0.953	0.971	0.510	0.750 (5)
EC-Earth3	0.574	0.170	0.466	0.732	0.594 (9)	0.886	0.074	0.966	0.990	0.260	0.872	0.074	0.949	0.971	0.344	0.271 (17)
EC-Earth3-CC	0.570	0.164	0.479	0.741	0.740 (5)	0.887	0.074	0.966	0.990	0.323	0.871	0.073	0.954	0.972	0.531	0.479 (14)
EC-Earth3-Veg	0.567	0.166	0.464	0.734	0.604 (8)	0.882	0.076	0.962	0.990	0.094	0.874	0.073	0.941	0.971	0.365	0.229 (19)
EC-Earth3-Veg-LR	0.556	0.177	0.425	0.711	0.073 (23)	0.882	0.077	0.963	0.990	0.104	0.867	0.077	0.947	0.968	0.073	0.083 (23)
FGOALS-g3	0.560	0.173	0.417	0.712	0.125 (22)	0.891	0.069	0.965	0.991	0.656	0.875	0.071	0.941	0.973	0.521	0.604 (10)
GFDL-CM4	0.591	0.162	0.495	0.752	0.906 (2)	0.891	0.070	0.967	0.991	0.708	0.882	0.068	0.962	0.975	0.927	0.833 (2)
GFDL-ESM4	0.569	0.169	0.451	0.728	0.448 (13)	0.889	0.073	0.966	0.991	0.427	0.883	0.067	0.960	0.976	0.948	0.688 (6)
INM-CM4-8	0.571	0.167	0.450	0.726	0.500 (12)	0.890	0.070	0.968	0.991	0.688	0.873	0.075	0.953	0.970	0.354	0.521 (11)
INM-CM5-0	0.570	0.174	0.442	0.719	0.292 (19)	0.888	0.072	0.968	0.991	0.531	0.874	0.074	0.956	0.971	0.479	0.458 (15)
IPSL-CM6A-LR	0.579	0.166	0.473	0.738	0.802 (4)	0.888	0.072	0.968	0.991	0.521	0.878	0.069	0.957	0.975	0.854	0.667 (7)
KIOST-ESM	0.547	0.167	0.443	0.725	0.333 (17)	0.881	0.077	0.963	0.989	0.052	0.870	0.075	0.954	0.970	0.302	0.125 (22)
MIROC6	0.570	0.168	0.453	0.731	0.573 (10)	0.894	0.071	0.968	0.991	0.667	0.878	0.073	0.953	0.971	0.563	0.667 (8)
MPI-ESM1-2-HR	0.578	0.170	0.438	0.719	0.354 (16)	0.888	0.071	0.968	0.991	0.594	0.878	0.071	0.951	0.973	0.708	0.667 (9)
MPI-ESM1-2-LR	0.577	0.173	0.431	0.715	0.302 (18)	0.888	0.071	0.968	0.991	0.594	0.873	0.073	0.950	0.972	0.490	0.500 (13)
MRI-ESM2-0	0.565	0.166	0.452	0.730	0.510 (11)	0.894	0.070	0.967	0.991	0.771	0.877	0.071	0.959	0.973	0.771	0.833 (3)
NESM3	0.566	0.167	0.448	0.725	0.417 (15)	0.886	0.072	0.965	0.991	0.323	0.871	0.075	0.945	0.970	0.167	0.208 (20)
NorESM2-LM	0.521	0.185	0.361	0.679	0.000 (24)	0.891	0.069	0.970	0.992	0.906	0.876	0.071	0.958	0.973	0.771	0.854 (1)
NorESM2-MM	0.559	0.170	0.418	0.714	0.167 (21)	0.888	0.073	0.967	0.991	0.385	0.870	0.076	0.953	0.969	0.198	0.271 (18)
TaiESM1	0.598	0.154	0.528	0.769	0.958 (1)	0.891	0.070	0.969	0.991	0.729	0.870	0.074	0.954	0.970	0.333	0.521 (12)

predictions. The rankings of the GCMs determined separately for the precipitation and temperature variables are presented in parentheses in Tables 2 and 3 for the use of linear scaling and distribution mapping, respectively.

The top-four ranked GCMs are selected as the members of the ensembles to be produced for each of the precipitation and temperature variables. The best-performing bias correction method and, hence, multi-model ensembles are determined by comparing the statistical performance metrics of the multi-model ensemble means observed using the linear scaling and distribution mapping methods for each climate variable, as detailed in Table 4. The statistical comparisons show that the best performing bias correction method is linear scaling for the precipitation variable and distribution mapping for the temperature variables. Accordingly, the members of the multi-model ensemble are GFDL-CM4, TaiESM1, CanESM5, and IPSL-CM6A-LR GCMs for the precipitation variable and NorESM2-LM, GFDL-CM4, MRI-ESM2-0, and BCC-CSM2-MR for the maximum and minimum temperature variables (Table 4). Similar to the findings of Ahmed *et al.* (2019), Bağçaci *et al.* (2021), Siqueira *et al.* (2021), and Seker and Gumus (2022) analysing the CMIP6 model performances for the cases of Pakistan, Turkey, a Brazilian Cerrado basin, and the Mediterranean Region of Turkey, respectively, the precipitation predictions of the multi-model ensemble do not have a highly close agreement with the observed records of the Bingol MS, contrary to the temperature predictions. Nevertheless, the statistical performances of the multi-model ensemble means (in Table 4) are higher than the individual performance metrics of each GCM for each climate variable (in Tables 2 and 3).

The mean monthly, seasonal, and annual total precipitation, maximum temperature, and minimum temperature predictions of the multi-model ensembles under the CMIP6 historical experiment are compared with the means of the observed records of the Bingol MS for the historical 1972–

1996 period and the 25-year means of the future periods attained under the emission scenarios of SSP245 and SSP585, as presented in Fig. 4. While the mean annual total precipitation, maximum temperature and minimum temperature rates of the historical records are 960.5 mm, 18.2°C, and 6.4°C, respectively, these means are determined in turn to be 937.2 mm, 18.1°C, and 6.2°C for the CMIP6 historical predictions (Fig. 4(a) and (b)). Under the SSP245 scenario, the mean annual total precipitation amount of the 2050–2075 period is 2.6% less than the mean of the CMIP6 historical predictions, and the differences in the mean precipitation amounts between the historical period and the near- and far-future periods are less than 1%. The mean annual maximum and minimum temperature differences between the historical and future periods gradually increase up to 4.6°C and 3.1°C, respectively (Fig. 4(b, c, e, g)). Under the SSP585 emission scenario, while there are no sharp differences in the mean annual total precipitation amounts between the historical period and near- and mid-future periods, the mean annual total precipitation amount of the 2075–2099 period is 9.2% less than the mean of the CMIP6 historical predictions. In addition, there is a gradual decrease in the mean autumn total precipitation amounts of the future periods, from 4.8% in 2025–2049 to 25.9% in 2075–2099 compared to the autumn mean of the CMIP6 historical predictions. The mean annual maximum and minimum temperature increases are more pronounced under the SSP585 scenario than in the SSP245. The gradual increases in the mean annual maximum and minimum temperatures reach 7.3°C and 5.3°C, respectively, in the 2075–2099 period (Fig. 4(b, d, f, h)).

3.2 Evaluation of the SWAT model performance

In the first and second steps of the model calibration process, two lapse rate parameters and six snow-related parameters, identified as sensitive according to the one-at-a-time

Table 4. Performance metrics of the multi-model ensemble means and selection of the best-performing bias correction method.

| Climate variable	Bias correction method	Selected GCMs	md	nRMSE	KGE	FSS
Precipitation	Linear scaling	GFDL-CM4 TaiESM1 CanESM5 IPSL-CM6A-LR	0.656	0.118	0.593	0.849
	Distribution mapping	TaiESM1 GFDL-CM4 CMCC-ESM2 IPSL-CM6A-LR	0.647	0.122	0.590	0.839
Maximum temperature	Linear scaling	INM-CM5-0 GFDL-ESM4 INM-CM4-8 NorESM2-LM	0.911	0.056	0.977	0.994
	Distribution mapping	NorESM2-LM GFDL-CM4 MRI-ESM2-0 BCC-CSM2-MR	0.913	0.056	0.980	0.994
Minimum temperature	Linear scaling	INM-CM5-0 GFDL-ESM4 INM-CM4-8 NorESM2-LM	0.900	0.058	0.967	0.982
	Distribution mapping	NorESM2-LM GFDL-CM4 MRI-ESM2-0 BCC-CSM2-MR	0.899	0.058	0.968	0.982
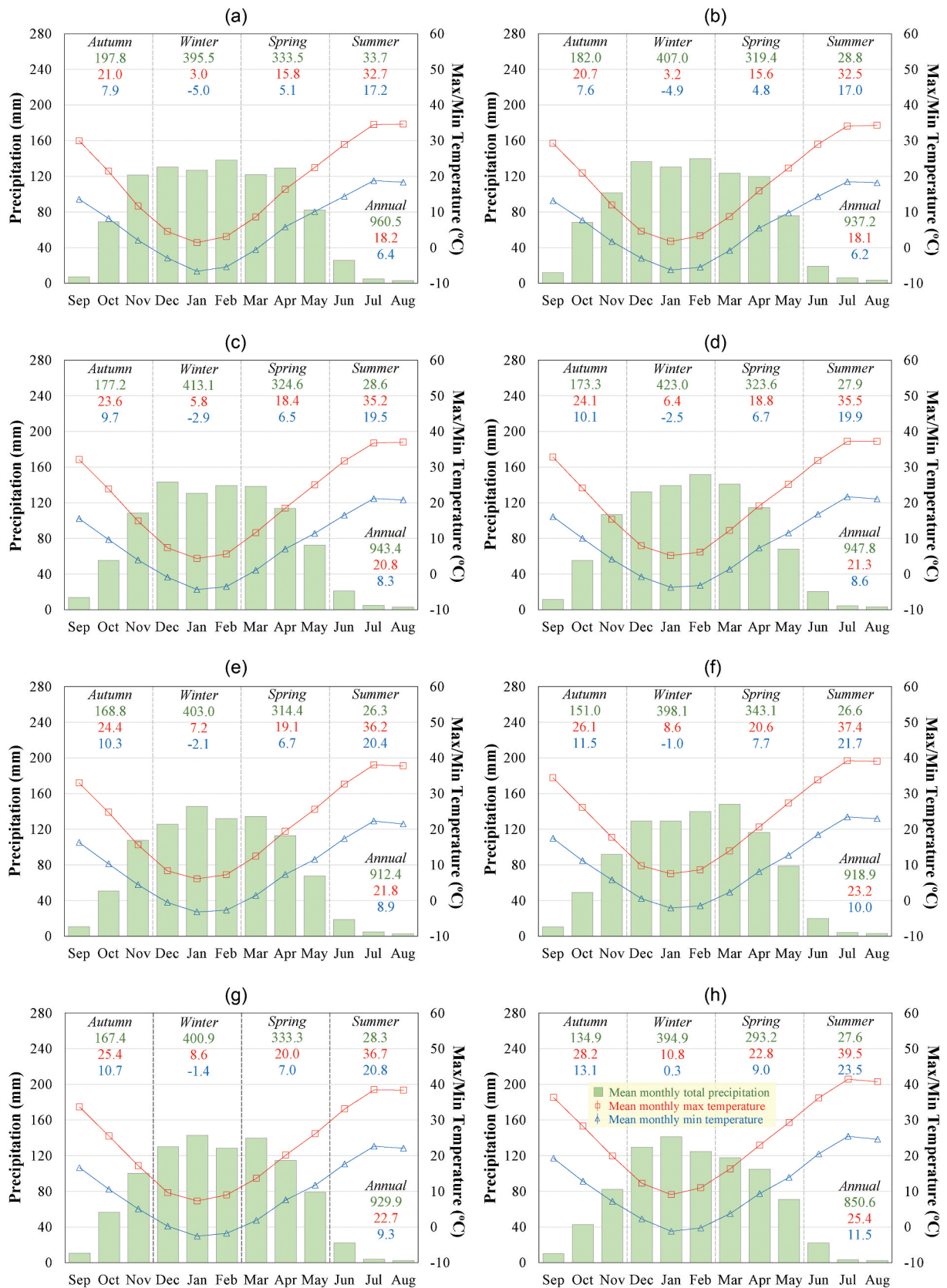
Figure 4. Comparison of the mean monthly, seasonal, and annual total precipitation and maximum/minimum temperature records of the Bingol station with the CMIP6 multi-model ensemble mean predictions: (a) observed climate data for the 1972–1996 period, (b) CMIP6 historical for the 1972–1996 period, (c) CMIP6 SSP245 for the 2025–2049 period, (d) CMIP6 SSP585 for the 2025–2049 period, (e) CMIP6 SSP245 for the 2050–2074 period, (f) CMIP6 SSP585 for the 2050–2074 period, (g) CMIP6 SSP245 for the 2075–2099 period, and (h) CMIP6 SSP585 for the 2075–2099 period.

sensitivity analyses, are fitted and then fixed to their best-performing parameter values, respectively. At the last step of the model calibration, a total of 11 sensitive modelling parameters related to groundwater, soil, hydrological response unit, management, and main channel are adjusted by repeating combined iterations two times. The parameters included in the three-stage calibration process are listed, starting from the most sensitive one for each step with their calibrated ranges and best-performing values, in Table 5. The observed and simulated monthly inflow rates of the Dipni reservoir in the calibration period of 1972–1988 are presented in Fig. 5(a). A P factor value of 0.88 and an R factor value of 1.03 are achieved for the calibrated parameter ranges, and the objective function NSE, br^2, PBIAS, and RSR statistics of the best simulation of the final combined iteration are found to be 0.83, 0.72, 3.03%, and 0.41, respectively, as detailed in Table 6.

The balance of R and P factors, which is recommended to be established with a minimum P factor value of 0.7 and an R factor value of around 1, is achieved by capturing a higher percentage of the observed data at approximately the same band thickness (Abbaspour *et al.* 2015b). According to Moriasi *et al.* (2007), an NSE value between 0.75 and 1, a PBIAS value less than ± 10%, and an RSR value less than 0.5 are collectively adequate to categorize the model calibration as very good in terms of monthly streamflow simulations. In addition, even though the slope of the linear regression line between the observed and simulated flow rates is slightly lower than the targeted value of around 1, the obtained value of 0.84 for the r^2 statistic, for which values greater than 0.6 are acceptable, is sufficient to support the conclusion that the calibrated model performance is very good (Santhi *et al.* 2001).

The monthly inflow simulations, obtained by executing the SWAT model with a single combined iteration using the calibrated parameter ranges in the validation period of 1989–1996,

are presented in Fig. 5(b). The simulation statistics of the validation period are given in Table 6. For the model validation, the calibrated parameter ranges provide a P factor value of 0.96 and an R factor value of 1.11, indicating the strength of the model calibration. The statistics of NSE, PBIAS, and RSR of the best simulation of the validation period are similar to the ones attained for the calibration period. Hence, the model performance in the validation period can be categorized as very good, as in the case of the calibration (Moriasi *et al.* 2007). However, the performance of the validation is not as good as that of the calibration in terms of the br^2 statistic. The decrease in br^2 from 0.72 to 0.59 is due to the declined slope of the linear regression line with the underestimated peak flows for some months of the validation period, as shown in Fig. 5(b). When the usability of the best-performing parameter set of the calibration in forecasting streamflow rates is analysed for the validation period, the statistical performance of the best simulation estimates is found to be similar to that of the best simulation of the validation, as detailed in Table 6. Moreover, when the forecasting performance of the calibrated SWAT model in terms of the M95PPU values is evaluated for both the calibration and validation periods (Fig. 5(a) and (b)), the model performance is found to be sufficient for all quantitative statistics (Table 6).

After verifying the forecasting performance of the calibrated SWAT model in terms of the best simulation estimates and M95PPU values, the effects of the utilized weather data are analysed for the whole historical period of 1972–1996 by comparing the SWAT model simulations performed with the observed weather data and CMIP6 historical predictions, as shown in Figs. 5(c) and 6(a), and Figs. 5(d) and 6(b), respectively. Due to the inability to obtain a close correlation between the precipitation records of the Bingol station and the CMIP6 historical precipitation predictions and the use of daily solar

Table 5. List of calibrated parameters.

Sensitive parameter[a]	Calibrated parameter range	Best-performing parameter value
Step 1: Calibration of precipitation and temperature lapse rates and fixing them to their best simulation values		
- Temperature lapse rate (°C/km), v__TLAPS.sub	−3.26[b]	
- Precipitation lapse rate (mm H_2O/km), v__PLAPS.sub	−8.82	
Step 2: Calibration of sensitive snow-related parameters and fixing them to their best simulation values		
- Snowfall temperature (°C), v__SFTMP.bsn	−0.17	
- Melt factor for snow on 21 December (mm H_2O/°C-day), v__SMFMN.bsn	1.474	
- Snow melt base temperature (°C), v__SMTMP.bsn	0.03	
- Snow pack temperature lag factor, v__TIMP.bsn	0.167	
- Minimum snow water content that corresponds to 100% snow cover (mm H_2O), v__SNOCOVMX.bsn	17.1	
- Melt factor for snow on 21 June (mm H_2O/°C-day), v__SMFMX.bsn	4.501	
Step 3: Calibration of other sensitive modelling parameters		
- Baseflow alpha factor (1/days), v__ALPHA_BF.gw	[0, 0.573]	0.093
- Depth from soil surface to bottom of layer (mm), r__SOL_Z().sol	[−0.7, 0.887]	−0.178
- Effective hydraulic conductivity in main channel alluvium (mm/h), v__CH_K2.rte	[−0.01, 323.295]	101.831
- Moist bulk density (mg/m³ or g/cm³), r__SOL_BD().sol	[0.075, 0.666]	0.424
- Initial SCS runoff curve number for moisture condition II, r__CN2.mgt	[−0.07, 0.043]	0.011
- Threshold depth of water in the shallow aquifer required for return flow to occur (mm H_2O), v__GWQMN.gw	[642.009, 3547.991]	2202.521
- Deep aquifer percolation fraction, v__RCHRG_DP.gw	[0, 0.618]	0.165
- Available water capacity of the soil layer (mm H_2O/ mm soil), r__SOL_AWC().sol	[4.101, 9.204]	8.74
- Groundwater delay time (days), v__GW_DELAY.gw	[71.7, 357.3]	113.683
- Groundwater *revap* coefficient, v__GW_REVAP.gw	[0.086, 0.2]	0.195
- Saturated hydraulic conductivity (mm/h), r__SOL_K().sol	[−0.99, 146.589]	72.652

[a]The qualifier (v__) refers to the substitution of a parameter with a value from the given range, while (r__) refers to a relative change in the parameter for which the current value is multiplied by 1 plus a factor in the given range.
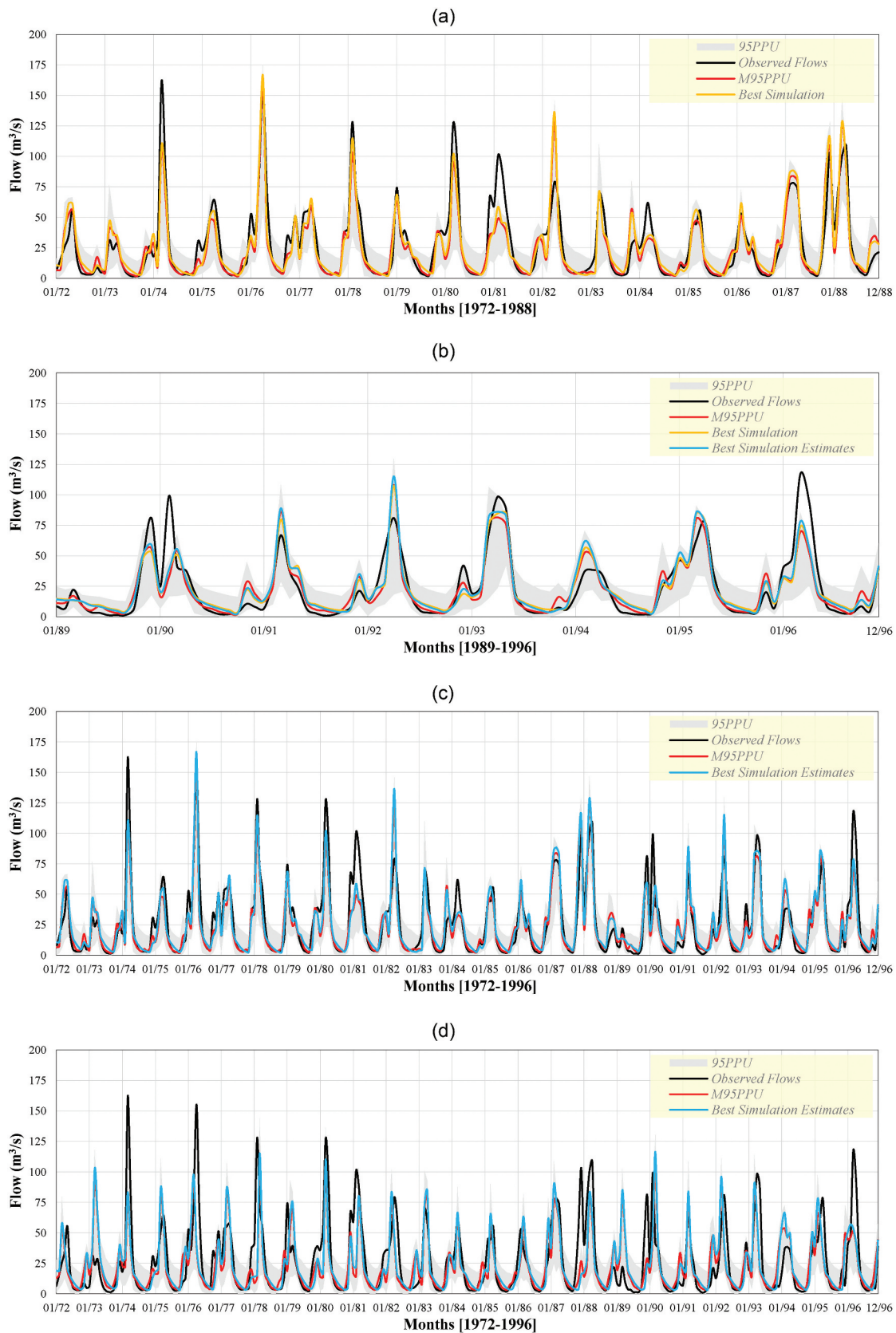[b]The fixed values indicate that a parameter is fitted and then fixed.

Figure 5. SWAT model simulation outputs: (a) calibrated model simulation for the 1972–1988 period, (b) calibrated model simulation for the validation period of 1989–1996, (c) calibrated model estimates for the 1972–1996 period obtained using the observed climate data, and (d) calibrated model estimates for the 1972–1996 period obtained using the CMIP6 historical predictions.

Table 6. List of the statistical performance indices obtained for the calibration and validation periods.

Model prediction	bR^2	b	NSE	PBIAS (%)	RSR	Mean_sim (Mean_obs)	StdDev_sim (StdDev_obs)
			Calibration period (1972–1988)				
Best simulation	0.72	0.86	0.83	3.03	0.41	26.73 (27.56)	27.95 (29.78)
M95PPU	0.67	0.81	0.82	9.49	0.43	24.95 (27.56)	26.57 (29.78)
			Validation period (1989–1996)				
Best simulation	0.59	0.74	0.79	−2.24	0.46	24.30 (23.77)	22.43 (26.77)
M95PPU	0.56	0.74	0.76	2.59	0.49	23.15 (23.77)	22.51 (26.77)
Best simulation estimates	0.62	0.79	0.78	−4.13	0.47	24.75 (23.77)	23.94 (26.77)

radiation, wind speed, and relative humidity rates produced by the SWAT weather generator, the monthly streamflow estimates obtained with the CMIP6 historical predictions are not as successful as the ones attained using the observed weather data. The underestimations in the peak flow rates simulated with the CMIP6 historical predictions are more pronounced than the ones simulated using the observed weather data. Nevertheless, as seen in the time series plots of Fig. 5(c) and (d), they are not systematic or specific to any month or season throughout the period. This increase in random underestimations could be explained as the loss of information on peak precipitation rates in averaging the bias corrected precipitation data of the best-performing top-four GCMs to produce the multi-model ensemble mean. The mean monthly, seasonal, and annual inflow estimates obtained with the CMIP6 historical predictions are relatively similar to the means of the observed inflows and the means of the estimates attained using the observed weather data (Fig. 6(a) and (b)). While the mean annual observed inflow rate of the Dipni reservoir is computed as 26.3 m³/s, the SWAT model simulations conducted with the observed weather data and CMIP6 historical predictions result in inflow rates of 26.1 and 24.4 m³/s for the best simulation estimates and 24.4 and 23.4 m³/s for the M95PPU values, respectively. Hence, the calibrated model estimates obtained using the CMIP6 historical predictions are appropriate for use as the baseline scenario to compare with the streamflow estimates attained under the future emission scenarios of SSP245 and SSP585.

The future inflow rates of the Dipni reservoir are forecasted in terms of both best simulation estimates and M95PPU values by performing the calibrated model simulations under the climate conditions of the SSP245 and SSP585 emission scenarios. The monthly flow estimates simulated using the CMIP6 SSP245 and CMIP6 SSP585 predictions are demonstrated within box-and-whisker plots in Fig. 6(c, e, g) and in Fig. 6(d, f, h) for the periods of 2025–2049, 2050–2074, and 2075–2099, respectively. The future flow estimates obtained for each forecasting approach are analysed in 25-year periods and intercompared by considering the estimates attained under the CMIP6 historical experiment as the baseline scenario, shown in Fig. 6(b). Accordingly, under the SSP245 scenario, while there are no significant differences in terms of the average annual inflow estimates between the historical and future periods, a gradual increase in the winter averages and a gradual decrease in the flows of the spring months are observed over the future period. The mean annual flow rates in terms of the best simulation

estimates and M95PPU values are 1.4%, 6.3%, and 5.7% less, and 2.0%, 6.4%, and 5.5% less, than the means of the historical period for the near-, mid-, and far-future periods, respectively. In terms of the best simulation estimates, while the mean flow rate in the spring season is decreased by 12.7% for the 2025–2049 period and 27.8% for the 2075–2099 period, the mean flow rate in the winter months is increased by 17.8% and 28.4%, respectively, in the same periods. Similar percentages are attained for the spring and winter means of the M95PPU values (Fig. 6(b, c, e, g)). Under the SSP585 scenario, the mean annual flow rates decrease gradually by up to 17.6% and 18.1% in the 2075–2099 period for the best simulation estimates and M95PPU values, respectively. For both flow forecasting approaches, gradual increases are observed in the autumn and spring averages. While the mean flow rates of the winter months in terms of the best simulation estimates and M95PPU values for the 2025–2049 period are 26.9% and 28.2% higher than the means in the historical period, respectively, they are 18.6% and 27.8% higher in turn for the 2075–2099 period (Fig. 6(b, d, f, h)). For both emission scenarios, the estimated flows in the snow accumulation months of January and February are much higher than the flows in the historical period, while the estimated flows for March and April, when the accumulated snow melts, are much less than the flows in the historical period. Since the future climate of the Dipni Basin tends to bring winter rain with rising temperatures, it could be said that precipitation will not fall as snow in the future winters as much as in the past.

3.3 Impacts of climate change on hydropower generation

There is a strong correlation, with an r^2 value of 0.97, between the long-term mean monthly total evaporation and temperature records of the Bingol MS, as presented in Fig. 7(a). By considering this relation to calculate monthly lake evaporation rates, the annual net evaporation amounts of the Dipni reservoir in the 1972–1996 period are computed as 531.8 and 526.8 mm, respectively, based on the station records and CMIP6 historical predictions (Fig. 7(b)). Under the SSP245 scenario, the annual net evaporation amounts increase to 640.2, 685.9, and 684.8 mm for the periods 2025–2049, 2050–2074, and 2075–2099, respectively (Fig. 7(c)). The increases are more pronounced under the SSP585 scenario, and amounts of 660.6, 727.2, and 818.0 mm are computed in turn for the same periods (Fig. 7(d)). Although the volume of water evaporated from the lake surface constitutes a small part of the total water budget of the Dipni reservoir, possible increases of up to about 55% in the annual net evaporation amount show the effects of
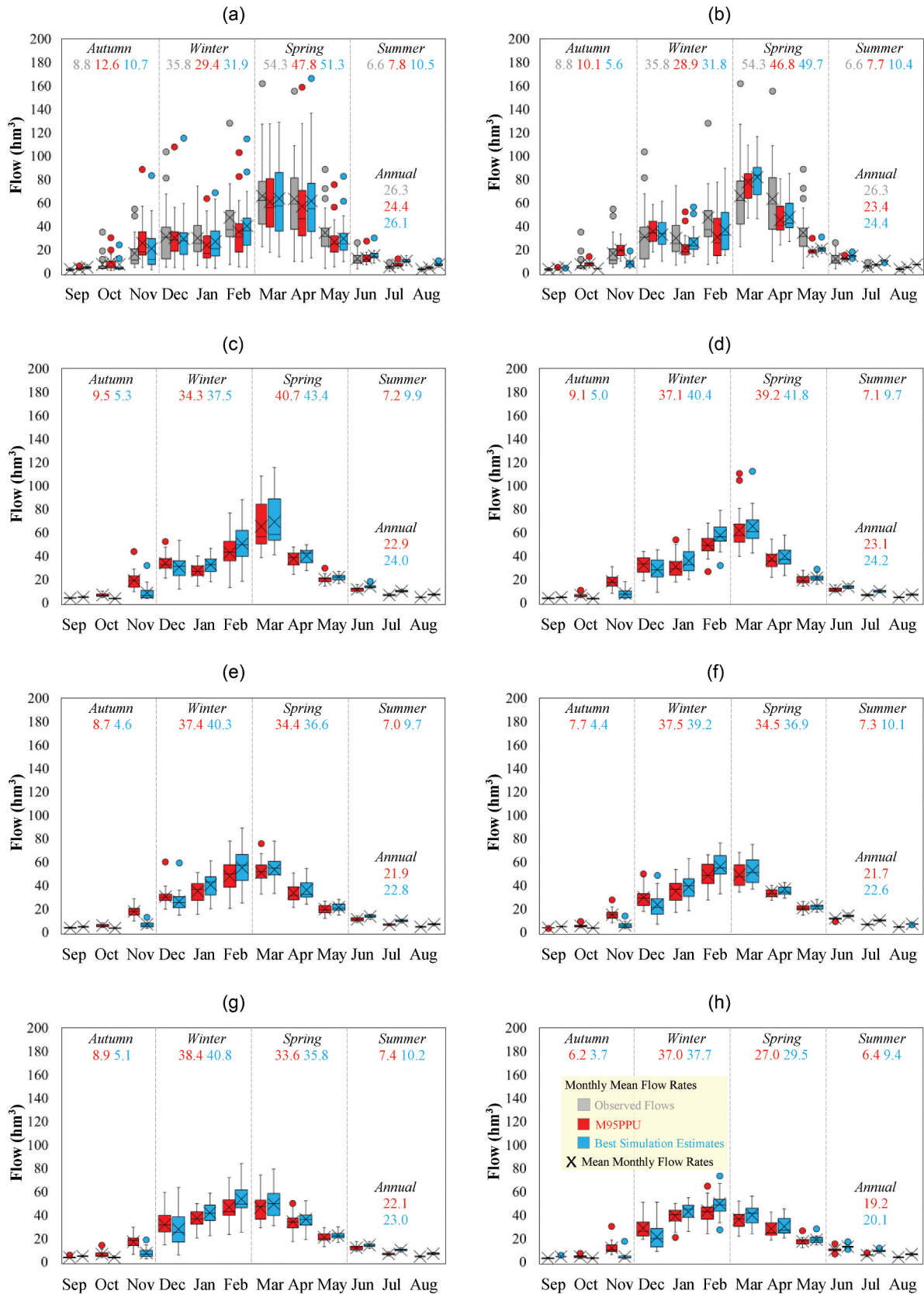
Figure 6. Mean monthly, seasonal, and annual flow estimates at the Dipni Dam location obtained through the SWAT model simulations using (a) observed climate data for the 1972–1996 period, (b) CMIP6 historical for the 1972–1996 period, (c) CMIP6 SSP245 for the 2025–2049 period, (d) CMIP6 SSP585 for the 2025–2049 period, (e) CMIP6 SSP245 for the 2050–2074 period, (f) CMIP6 SSP585 for the 2050–2074 period, (g) CMIP6 SSP245 for the 2075–2099 period, and (h) CMIP6 SSP585 for the 2075–2099 period.

increasing temperatures and decreasing precipitation trends in the Dipni Basin.

The results of the 25-year reservoir operations conducted in the past and three future periods, with the changing inputs of monthly flow estimates and lake evaporation rates, are summarized in Table 7. Accordingly, for the historical period, the mean annual total energy production is determined to be 202.7 GWh/year using the lake evaporations based on the observed climate data and the observed inflows as the inputs of the operation algorithm. The use of the best simulation estimates and M95PPU values simulated with the observed climate data instead of the observed inflows in the operation algorithm results in total energy production values of 208.5 and 195.5 GWh/year, respectively. When the inflow estimates and lake evaporation values determined based on the CMIP historical predictions are utilized as the inputs of the operation algorithm, the mean annual total energy productions are computed as 199.3 and 192.6 GWh/year using the best simulation estimates and M955PPU values, respectively. In addition, it is observed that the underestimated peak flows of the SWAT model simulations result in significant decreases in the number and amount of spillway releases. Nevertheless, similar firm discharges, power releases, and firm and secondary energy productions could be obtained in all reservoir operations of the historical period, as detailed in Table 7. Since the Dipni

Dam is not yet in operation, the reservoir operation results obtained using the inflow and lake evaporation estimates based on the CMIP historical predictions are used as the historical baseline scenario for comparisons with the operation results of the future periods.

According to the reservoir operations conducted under the SSP245 scenario, a major decrease in the amount of energy produced is attained for the mid-future period. In this period, the energy produced is 8.9% and 10.1% less than the energy production obtained under the CMIP6 historical experiment, based on the use of the best simulation estimates and M95PPU values, respectively (Table 7). Under the SSP585 scenario, the energy production of the Dipni HEPP declines abruptly after the near-future period. While the energy production values decrease by 9.4% and 11.2% in the 2050–2074 period, with the use of the best simulation estimates and M95PPU values, respectively, the decrease ratios are found to be 20.1% and 21.5% in turn for the 2075–2099 period (Table 7). In the feasibility report for the Dipni Project, the total energy production is declared as 204.2 GWh/year, with 199.6 GWh/year of firm energy and 4.6 GWh/year of secondary energy (EN-SU 2008). Regardless of which future scenario or which flow forecasting approach is evaluated, it is undoubtedly clear that the expected economic benefit from the Dipni Project, which is economically and technically designed by
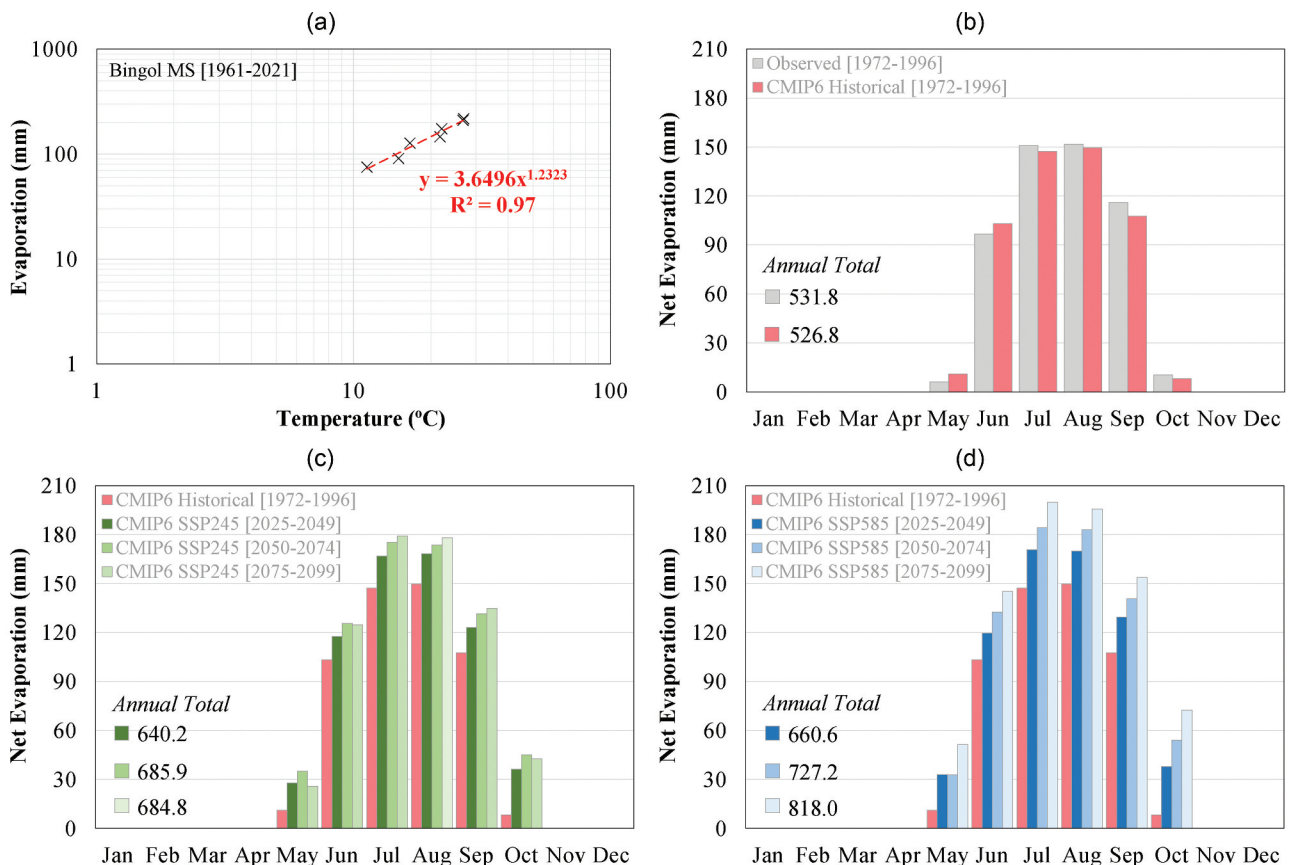

Figure 7. (a) Correlation between the mean monthly total evaporation and temperature records of the Bingol station, and comparison of the monthly net evaporation rates of the Dipni reservoir calculated using (b) observed climate data and CMIP6 historical predictions, (c) CMIP6 historical and CMIP6 SSP245 predictions, and (d) CMIP6 historical and CMIP6 SSP585 predictions.

Table 7. Operation results for the Dipni Dam and HEPP Project under historical and future climate conditions.

Climate data		Observed			CMIP6 historical		CMIP6 SSP245						CMIP6 SSP585				
Operation period		1972–1996			1972–1996		2025–2049		2050–2074		2075–2099		2025–2049		2050–2074		2075–2099
Flow data		Observed	M9SPPU	Best simulation estimates	M9SPPU	Best simulation estimates	M9SPPU	Best simulation estimates	M9SPPU	Best simulation estimates	M9SPPU	Best simulation estimates	M9SPPU	Best simulation estimates	M9SPPU	Best simulation estimates	M9SPPU	Best simulation estimates
Inflow	m³/s	26.3	24.4	26.1	23.4	24.4	22.9	24.0	21.9	22.8	22.1	23.0	23.1	24.2	21.7	22.6	19.2	20.1
	hm³/year	827.6	767.5	820.4	737.3	767.8	720.0	753.9	686.6	715.1	693.0	720.6	726.1	759.3	681.4	709.4	600.7	628.8
Evaporation	hm³/year	1.6	1.5	1.5	1.5	1.5	1.7	1.8	1.8	1.8	2.1	2.1	1.7	1.6	1.7	1.8	2.5	2.5
Non-power release	hm³/year	84.8	84.8	84.8	84.8	84.8	84.8	84.8	84.8	84.8	84.8	84.8	84.8	84.8	84.8	84.8	84.8	84.8
Spillway release	month	18	5	6	4	5	11	13	8	8	5	6	3	3	3	4	10	10
	m³/s	30.9	38.2	38.6	4.2	8.1	10.9	11.6	13.7	17.0	12.1	15.0	33.1	40.0	13.0	13.6	9.3	12.3
	hm³/year	58.2	20.2	24.3	1.8	4.2	12.7	15.9	11.2	13.9	6.3	9.4	10.5	12.6	4.0	5.5	9.7	12.8
Power release	m³/s	22.3	21.9	23.4	21.5	22.3	20.6	21.6	19.6	20.4	20.0	20.7	20.9	21.9	19.7	20.5	16.9	17.7
	hm³/year	704.5	689.5	737.0	677.2	705.3	649.2	680.5	618.1	644.2	629.5	653.9	658.0	689.6	620.5	646.9	533.3	558.4
Firm discharge	m³/s	22.6	22.1	23.7	21.8	22.9	20.8	21.9	19.9	20.9	20.4	21.2	21.3	22.5	20.1	21.0	17.0	17.9
Regulation ratio	%	85.1	89.8	89.8	91.8	91.9	90.2	90.3	90.0	90.1	90.8	90.7	90.6	90.8	91.1	91.2	88.8	88.8
Firm energy	GWh/year	195.9	189.1	201.9	187.1	194.7	178.4	187.3	167.6	177.0	179.6	188.2	180.2	187.4	166.6	176.4	144.5	153.6
Secondary energy	GWh/year	6.8	6.5	6.6	5.5	4.6	5.7	6.2	5.6	4.5	4.2	4.7	4.8	3.5	4.4	4.0	6.5	5.6
Total energy	GWh/year	202.7	195.5	208.5	192.6	199.3	184.2	193.5	173.2	181.5	183.8	192.9	185.0	190.9	171.1	180.5	151.1	159.2

optimizing the installed power capacity based on the historical flow observations, cannot be met in the future due to the changing climate conditions in the basin.

4 Summary and conclusions

This study investigates how global warming affects streamflow, lake evaporation, and hydropower production in the most threatened highlands region of the Euphrates-Tigris Basin, using the example of the Dipni Dam and HEPP Project. The results of this assessment can be summarized in six main points: (1) the mean annual maximum and minimum temperature rates gradually increase by up to 4.6 and 3.1°C under the SSP245 scenario and up to 7.3 and 5.3°C under the SSP585 scenario, through the future period; (2) the mean annual total precipitation amount decreases by 2.6% in the mid-future period under the SSP245 scenario and 9.2% in the far-future period under the SSP585 scenario; (3) while the projected changes in the future precipitation and temperature rates result in decrease by about a 6% in the mean annual inflow rate of the Dipni reservoir after the near-future period under the SSP245 scenario, a gradual decrease reaching about 18% in the far-future period is observed for the mean annual inflow rate under the SSP585 scenario; (4) the gradual increases in the winter flows and gradual decreases in the flows of the spring months through the future period show the impact of the warming climate on the hydrological regime of this snow-fed basin for both emission scenarios; (5) possible increases of up to about 30% and 55%, respectively, under the SSP245 and SSP585 emission scenarios are detected in the annual net evaporation amount of the Dipni reservoir; (6) all these projected changes in the hydro-climatic regime of the Dipni Basin result in possible decreases of up to 10.1% and 21.5% in the total energy production of the project under the SSP245 and SSP585 scenarios, respectively.

The results of the operation studies conducted indicate the need for adaptive measures against the changing climate. While there are no significant changes in terms of regulation ratio and secondary energy production through the future period, considerable decreases are determined in the firm discharge rate and, hence, firm energy production, particularly for the SSP585 scenario after the first half of the century. Due to the underestimation problem in the peak flow simulations of the SWAT model, consistent outcomes could not be obtained in terms of the spillway usage statistics. For this purpose, further work should be undertaken to increase the performance of the precipitation predictions of the multi-model ensemble by trying different bias correction methods and averaging approaches in producing ensemble means (Kim et al. 2016, Tumsa 2022). To conclude, there is a clear need to inform the riparian countries about changing hydro-climatic conditions and their impacts on hydropower production, and it is thought that the results of this assessment will help increase awareness about the necessity of implementing effective adaptation measures in the Euphrates-Tigris Basin.

Disclosure statement

No potential conflict of interest was reported by the author.

ORCID

Emrah Yalcin http://orcid.org/0000-0002-3742-8866

References

Abbaspour, K.C., *et al.*, 2007. Modelling hydrology and water quality in the pre-alpine/alpine Thur watershed using SWAT. *Journal of Hydrology*, 333 (2–4), 413–430. doi:10.1016/j.jhydrol.2006.09.014.

Abbaspour, K.C., 2015a. *SWAT-CUP2: SWAT calibration and uncertainty programs - a user manual*. Duebendorf, Switzerland: Eawag - Swiss Federal Institute of Aquatic Science and Technology.

Abbaspour, K.C., *et al.*, 2015b. A continental-scale hydrology and water quality model for Europe: calibration and uncertainty of a high-resolution large-scale SWAT model. *Journal of Hydrology*, 524, 733–752. doi:10.1016/j.jhydrol.2015.03.027.

Abbaspour, K.C., Johnson, C.A., and van Genuchten, M.T., 2004. Estimating uncertain flow and transport parameters using a sequential uncertainty fitting procedure. *Vadose Zone Journal*, 3 (4), 1340–1352. doi:10.2136/vzj2004.1340.

Adam, J.C., Hamlet, A.F., and Lettenmaier, D.P., 2009. Implications of global climate change for snowmelt hydrology in the twenty-1st century. *Hydrological Processes*, 23 (7), 962–972. doi:10.1002/hyp.7201.

Ahmed, K., *et al.*, 2019. Selection of multi-model ensemble of general circulation models for the simulation of precipitation and maximum and minimum temperature based on spatial assessment metrics. *Hydrology and Earth System Sciences*, 23 (11), 4803–4824. doi:10.5194/hess-23-4803-2019.

Almeida, M.P., Perpiñán, O., and Narvarte, L., 2015. PV power forecast using a nonparametric PV model. *Solar Energy*, 115, 354–368. doi:10.1016/j.solener.2015.03.006

Arnold, J.G., *et al.*, 2013. *SWAT 2012 input/output documentation*. Texas: Texas Water Resources Institute.

Bağçaci, S.Ç., *et al.*, 2021. Intercomparison of the expected change in the temperature and the precipitation retrieved from CMIP6 and CMIP5 climate projections: a Mediterranean hot spot case, Turkey. *Atmospheric Research*, 256, 105576. doi:10.1016/j.atmosres.2021.105576.

Barnett, T.P., Adam, J.C., and Lettenmaier, D.P., 2005. Potential impacts of a warming climate on water availability in snow-dominated regions. *Nature*, 438, 303–309. doi:10.1038/nature04141

Bentsen, M., *et al.*, 2019a. *NCC NorESM2-MM model output prepared for CMIP6 CMIP historical*. Earth System Grid Federation. doi:10.22033/ESGF/CMIP6.8040.

Bentsen, M., *et al.*, 2019b. *NCC NorESM2-MM model output prepared for CMIP6 ScenarioMIP ssp245 and ScenarioMIP ssp585*. Earth System Grid Federation. doi:10.22033/ESGF/CMIP6.608.

Boisrame, G., 2011. *WGNmaker4.1.xlsm Microsoft Excel macro* [online]. Available from: https://swat.tamu.edu/software/ [Accessed 2 July 2022].

Boucher, O., *et al.*, 2018. *IPSL IPSL-CM6A-LR model output prepared for CMIP6 CMIP historical*. Earth System Grid Federation. doi:10.22033/ESGF/CMIP6.5195.

Boucher, O., *et al.*, 2019. *IPSL IPSL-CM6A-LR model output prepared for CMIP6 ScenarioMIP ssp245 and ScenarioMIP ssp585*. Earth System Grid Federation. doi:10.22033/ESGF/CMIP6.1532.

Bozkurt, D. and Sen, O.L., 2013. Climate change impacts in the Euphrates-*Tigris* Basin based on different model and scenario simulations. *Journal of Hydrology*, 480, 149–161. doi:10.1016/j.jhydrol.2012.12.021

Cao, J., 2019. *NUIST NESMv3 model output prepared for CMIP6 ScenarioMIP ssp245 and ScenarioMIP ssp585*. Earth System Grid Federation. doi:10.22033/ESGF/CMIP6.2027.

Cao, J. and Wang, B., 2019. *NUIST NESMv3 model output prepared for CMIP6 CMIP historical*. Earth System Grid Federation. doi:10.22033/ESGF/CMIP6.8769.

Chen, J., *et al.*, 2013. Finding appropriate bias correction methods in downscaling precipitation for hydrologic impact studies over North America. *Water Resources Research*, 49 (7), 4187–4205. doi:10.1002/wrcr.20331.

Chen, W., Jiang, Z., and Li, L., 2011. Probabilistic projections of climate change over China under the SRES A1B scenario using 28 AOGCMs. *Journal of Climate*, 24 (17), 4741–4756. doi:10.1175/2011JCLI4102.1.

Chenoweth, J., *et al.*, 2011. Impact of climate change on the water resources of the eastern Mediterranean and Middle East region: modeled 21st century changes and implications. *Water Resources Research*, 47 (6), W06506. doi:10.1029/2010WR010269.

Cygwin, 2022. *Cygwin user's guide* [online]. Available from: https://www.cygwin.com/cygwin-ug-net/cygwin-ug-net.pdf [Accessed 20 May 2022].

Daggupati, P., *et al.*, 2017. Spatial and temporal patterns of precipitation and stream flow variations in Tigris-*Euphrates* river basin. *Environmental Monitoring and Assessment*, 189 (2), 50. doi:10.1007/s10661-016-5752-y.

Dix, M., *et al.*, 2019a. *CSIRO-ARCCSSACCESS-CM2 model output prepared for CMIP6 CMIP historical*. Earth System Grid Federation. doi:10.22033/ESGF/CMIP6.4271.

Dix, M., *et al.*, 2019b. *CSIRO-ARCCSSACCESS-CM2 model output prepared for CMIP6 ScenarioMIP ssp245 and ScenarioMIP ssp585*. Earth System Grid Federation. doi:10.22033/ESGF/CMIP6.2285.

DSI (General Directorate of State Hydraulic Works), 2022. *Electrical power resources survey and development administration (EIE) - flow gauging yearbooks (1935-2011)*. Ankara: General Directorate of State Hydraulic Works.

Duratorre, T., *et al.*, 2020. Hydropower potential in the Alps under climate change scenarios: the Chavonne Plant, Val D'Aosta. *Water*, 12 (7), 2011. doi:10.3390/w12072011.

EC-Earth (EC-Earth Consortium), 2019a. *EC-Earth-Consortium EC-Earth3 model output prepared for CMIP6 CMIP historical*. Earth System Grid Federation. doi:10.22033/ESGF/CMIP6.4700.

EC-Earth (EC-Earth Consortium), 2019b. *EC-Earth-Consortium EC-Earth3 model output prepared for CMIP6 ScenarioMIP ssp245 and ScenarioMIP ssp585*. Earth System Grid Federation. doi:10.22033/ESGF/CMIP6.251.

EC-Earth (EC-Earth Consortium), 2019c. *EC-Earth-Consortium EC-Earth3-Veg model output prepared for CMIP6 CMIP historical*. Earth System Grid Federation. doi:10.22033/ESGF/CMIP6.4706.

EC-Earth (EC-Earth Consortium), 2019d. *EC-Earth-Consortium EC-Earth3-Veg model output prepared for CMIP6 ScenarioMIP ssp245 and ScenarioMIP ssp585*. Earth System Grid Federation. doi:10.22033/ESGF/CMIP6.727.

EC-Earth (EC-Earth Consortium), 2020a. *EC-Earth-Consortium EC-Earth3-Veg-LR model output prepared for CMIP6 CMIP historical*. Earth System Grid Federation. doi:10.22033/ESGF/CMIP6.4707.

EC-Earth (EC-Earth Consortium), 2020b. *EC-Earth-Consortium EC-Earth3-Veg-LR model output prepared for CMIP6 ScenarioMIP ssp245 and ScenarioMIP ssp585*. Earth System Grid Federation. doi:10.22033/ESGF/CMIP6.728.

EC-Earth (EC-Earth Consortium), 2021a. *EC-Earth-Consortium EC-Earth-3-CC model output prepared for CMIP6 CMIP historical*. Earth System Grid Federation. doi:10.22033/ESGF/CMIP6.4702.

EC-Earth (EC-Earth Consortium), 2021b. *EC-Earth-Consortium EC-Earth-3-CC model output prepared for CMIP6 ScenarioMIP ssp245 and ScenarioMIP ssp585*. Earth System Grid Federation. doi:10.22033/ESGF/CMIP6.15327.

EC-JRC (European Commission - Joint Research Centre), 2006. *The Global Land Cover 2000 (GLC2000) products* [online]. Available from: https://forobs.jrc.ec.europa.eu/products/glc2000/products.php [Accessed 28 June 2022].

Ehsani, N., *et al.*, 2017. Reservoir operations under climate change: storage capacity options to mitigate risk. *Journal of Hydrology*, 555, 435–446. doi:10.1016/j.jhydrol.2017.09.008.

EN-SU (EN-SU Engineering and Consultancy Limited Company), 2008. *The Dipni Dam and HEPP project feasibility report*. Ankara: EN-SU Engineering and Consultancy Limited Company.

ESGF (Earth System Grid Federation), 2022. *WCRP coupled model inter-comparison project (Phase 6)* [online]. Available from: https://esgf-node.llnl.gov/projects/cmip6/ [Accessed 15 May 2022].

FAO (Food and Agriculture Organization of the United Nations), 2007. *Digital Soil Map of the World (DSMW)* [online]. Available from: https://www.fao.org/geonetwork/srv/en/metadata.show?id=14116 [Accessed 28 June 2022].

Farsani, I.F., *et al.*, 2019. Assessment of the impact of climate change on spatiotemporal variability of blue and green water resources under CMIP3 and CMIP5 models in a highly mountainous watershed. *Theoretical and Applied Climatology*, 136, 169–184. doi:10.1007/s00704-018-2474-9.

FPGA (Euphrates Planning Group Authority), 1968. *The Tigris Basin reconnaissance report*. Ankara: General Directorate of State Hydraulic Works - Euphrates Planning Group Authority.

Giorgi, F., 2006. Climate change hot-spots. *Geophysical Research Letters*, 33 (8), L08707. doi:10.1029/2006GL025734.

Guo, H., *et al.*, 2018a. *NOAA-GFDLGFDL-CM4 model output prepared for CMIP6 CMIP historical*. Earth System Grid Federation. doi:10.22033/ESGF/CMIP6.8594.

Guo, H., *et al.*, 2018b. *NOAA-GFDLGFDL-CM4 model output prepared for CMIP6 ScenarioMIP ssp245 and ScenarioMIP ssp585*. Earth System Grid Federation. doi:10.22033/ESGF/CMIP6.9242.

Gupta, H.V., *et al.*, 2009. Decomposition of the mean squared error and NSE performance criteria: implications for improving hydrological modelling. *Journal of Hydrology*, 377 (1–2), 80–91. doi:10.1016/j.jhydrol.2009.08.003.

Hasson, S.U., 2016. Future water availability from Hindukush-Karakoram-Himalaya upper Indus Basin under conflicting climate change scenarios. *Climate*, 4 (3), 40. doi:10.3390/cli4030040.

IPCC (Intergovernmental Panel on Climate Change), 2021. Summary for policymakers. *In*: V. Masson-Delmotte, *et al.*, eds. *Climate change 2021: the physical science basis. Contribution of working group I to the IPCC sixth assessment report*. Cambridge and New York: Cambridge University Press, 3–32.

John, J.G., *et al.*, 2018. *NOAA-GFDLGFDL-ESM4 model output prepared for CMIP6 ScenarioMIP ssp245 and ScenarioMIP ssp585*. Earth System Grid Federation. doi:10.22033/ESGF/CMIP6.1414.

Jones, P.W., 1999. First- and second-order conservative remapping schemes for grids in spherical coordinates. *Monthly Weather Review*, 127 (9), 2204–2210. doi:10.1175/1520-0493(1999)127<2204:FASOCR>2.0.CO;2.

Jungclaus, J., *et al.*, 2019. *MPI-M MPI-ESM1.2-HR model output prepared for CMIP6 CMIP historical*. Earth System Grid Federation. doi:10.22033/ESGF/CMIP6.6594.

Kim, J., Ivanov, V.Y., and Fatichi, S., 2016. Climate change and uncertainty assessment over a hydroclimatic transect of Michigan. *Stochastic Environmental Research and Risk Assessment*, 30, 923–944. doi:10.1007/s00477-015-1097-2

Kim, Y.H., *et al.*, 2019a. *KIOST KIOST-ESM model output prepared for CMIP6 CMIP historical*. Earth System Grid Federation. doi:10.22033/ESGF/CMIP6.5296.

Kim, Y.H., *et al.*, 2019b. *KIOST KIOST-ESM model output prepared for CMIP6 ScenarioMIP ssp245 and ScenarioMIP ssp585*. Earth System Grid Federation. doi:10.22033/ESGF/CMIP6.11241.

Kitoh, A., Yatagai, A., and Alpert, P., 2008. First super-high-resolution model projection that the ancient "Fertile Crescent" will disappear in this century. *Hydrological Research Letters*, 2, 1–4. doi:10.3178/hrl.2.1.

Krasting, J.P., *et al.*, 2018. *NOAA-GFDLGFDL-ESM4 model output prepared for CMIP6 CMIP historical*. Earth System Grid Federation. doi:10.22033/ESGF/CMIP6.8597.

Lee, W.-L. and Liang, H.-C., 2020a. *AS-RCEC TaiESM1.0 model output prepared for CMIP6 CMIP historical*. Earth System Grid Federation. doi:10.22033/ESGF/CMIP6.9755.

Lee, W.-L. and Liang, H.-C., 2020b. *AS-RCEC TaiESM1.0 model output prepared for CMIP6 ScenarioMIP ssp245 and ScenarioMIP ssp585*. Earth System Grid Federation. doi:10.22033/ESGF/CMIP6.9688.

Legates, D.R. and McCabe, G.J., 1999. Evaluating the use of "goodness-of-fit" measures in hydrologic and hydroclimatic model validation. *Water Resources Research*, 35 (1), 233–241. doi:10.1029/1998WR900018.

Lelieveld, J., *et al.*, 2012. Climate change and impacts in the Eastern Mediterranean and the Middle East. *Climatic Change*, 114 (3–4), 667–687. doi:10.1007/s10584-012-0418-4.

Lemann, T., Roth, V., and Zeleke, G., 2017. Impact of precipitation and temperature changes on hydrological responses of small-scale

catchments in the Ethiopian Highlands. *Hydrological Sciences Journal*, 62 (2), 270–282. doi:10.1080/02626667.2016.1217415.

Li, L., 2019a. *CAS FGOALS-g3 model output prepared for CMIP6 CMIP historical*. Earth System Grid Federation. doi:10.22033/ESGF/CMIP6.3356.

Li, L., 2019b. *CAS FGOALS-g3 model output prepared for CMIP6 ScenarioMIP ssp245 and ScenarioMIP ssp585*. Earth System Grid Federation. doi:10.22033/ESGF/CMIP6.2056.

Liersch, S., 2003. *Dewpoint estimation programs: dew.exe and dew02.exe* [online]. Available from: https://swat.tamu.edu/software/ [Accessed 2 July 2022].

Lovato, T., Peano, D., and Butenschön, M., 2021a. *CMCC CMCC-ESM2 model output prepared for CMIP6 CMIP historical*. Earth System Grid Federation. doi:10.22033/ESGF/CMIP6.13195.

Lovato, T., Peano, D., and Butenschön, M., 2021b. *CMCC CMCC-ESM2 model output prepared for CMIP6 ScenarioMIP ssp245 and ScenarioMIP ssp585*. Earth System Grid Federation. doi:10.22033/ESGF/CMIP6.13168.

MGM (Turkish State Meteorological Service), 2022a. *Annual maximum precipitation records in standard times for the Bingol meteorological station*. Ankara: Turkish State Meteorological Service.

MGM (Turkish State Meteorological Service), 2022b. *Daily precipitation, maximum and minimum air temperature, solar radiation, wind speed, and relative humidity records of the Bingol meteorological station*. Ankara: Turkish State Meteorological Service.

MGM (Turkish State Meteorological Service), 2022c. *Long-term all parameters bulletin for the Bingol meteorological station*. Ankara: Turkish State Meteorological Service.

Miao, C., *et al.*, 2012. On the applicability of temperature and precipitation data from CMIP3 for China. *PLoS ONE*, 7 (9), e44659. doi:10.1371/journal.pone.0044659.

Moriasi, D.N., *et al.*, 2007. Model evaluation guidelines for systematic quantification of accuracy in watershed simulations. *Transactions of the ASABE*, 50 (3), 885–900. doi:10.13031/2013.23153.

Nash, J.E. and Sutcliffe, J.V., 1970. River flow forecasting through conceptual models part I - a discussion of principles. *Journal of Hydrology*, 10 (3), 282–290. doi:10.1016/0022-1694(70)90255-6.

Nazeer, A., *et al.*, 2022. Changes in the hydro-climatic regime of the Hunza Basin in the Upper Indus under CMIP6 climate change projections. *Scientific Reports*, 12, 21442. doi:10.1038/s41598-022-25673-6.

Neitsch, S.L., *et al.*, 2011. *Soil and water assessment tool theoretical documentation version 2009*. Texas: Texas Water Resources Institute.

Nilsson, C., *et al.*, 2005. Fragmentation and flow regulation of the world's large river systems. *Science*, 308 (5720), 405–408. doi:10.1126/science.1107887.

Nohara, D., *et al.*, 2006. Impact of climate change on river discharge projected by multimodel ensemble. *Journal of Hydrometeorology*, 7 (5), 1076–1089. doi:10.1175/JHM531.1.

O'Neill, B.C., *et al.*, 2016. The scenario model intercomparison project (ScenarioMIP) for CMIP6. *Geoscientific Model Development*, 9 (9), 3461–3482. doi:10.5194/gmd-9-3461-2016.

Özdoğan, M., 2011. Climate change impacts on snow water availability in the Euphrates-Tigris basin. *Hydrology and Earth System Sciences*, 15 (9), 2789–2803. doi:10.5194/hess-15-2789-2011.

Qin, P., *et al.*, 2022. Projected impacts of climate change on major dams in the Upper Yangtze River Basin. *Climatic Change*, 170 (1–2), 8. doi:10.1007/s10584-021-03303-w.

Rathjens, H., *et al.*, 2016. *CMhyd user manual: documentation for preparing simulated climate change data for hydrologic impact studies* [online]. Available from: https://swat.tamu.edu/media/115265/bias_cor_man.pdf [Accessed 25 May 2022].

Roberts, N.M. and Lean, H.W., 2008. Scale-selective verification of rainfall accumulations from high-resolution forecasts of convective events. *Monthly Weather Review*, 136 (1), 78–97. doi:10.1175/2007MWR2123.1.

Santhi, C., *et al.*, 2001. Validation of the SWAT model on a large river basin with point and nonpoint sources. *Journal of the American Water Resources Association*, 37 (5), 1169–1188. doi:10.1111/j.1752-1688.2001.tb03630.x.

Schulzweida, U., 2021. *CDO user guide version 2.0.5*. Hamburg: Max Planck Institute for Meteorology.

Schupfner, M., *et al.*, 2019. *DKRZ MPI-ESM1.2-HR model output prepared for CMIP6 ScenarioMIP ssp245 and ScenarioMIP ssp585*. Earth System Grid Federation. doi:10.22033/ESGF/CMIP6.2450.

Seker, M. and Gumus, V., 2022. Projection of temperature and precipitation in the Mediterranean region through multi-model ensemble from CMIP6. *Atmospheric Research*, 280, 106440. doi:10.1016/j.atmosres.2022.106440

Seland, Ø., *et al.*, 2019a. *NCC NorESM2-LM model output prepared for CMIP6 CMIP historical*. Earth System Grid Federation. doi:10.22033/ESGF/CMIP6.8036.

Seland, Ø., *et al.*, 2019b. *NCC NorESM2-LM model output prepared for CMIP6 ScenarioMIP ssp245 and ScenarioMIP ssp585*. Earth System Grid Federation. doi:10.22033/ESGF/CMIP6.604.

Şen, Z., 2019. Climate change expectations in the upper Tigris River basin, Turkey. *Theoretical and Applied Climatology*, 137, 1569–1585. doi:10.1007/s00704-018-2694-z.

Shiogama, H., Abe, M., and Tatebe, H., 2019. *MIROC MIROC6 model output prepared for CMIP6 ScenarioMIP ssp245 and ScenarioMIP ssp585*. Earth System Grid Federation. doi:10.22033/ESGF/CMIP6.898.

Siqueira, P.P., *et al.*, 2021. Effects of climate and land cover changes on water availability in a Brazilian Cerrado basin. *Journal of Hydrology: Regional Studies*, 37, 100931. doi:10.1016/j.ejrh.2021.100931.

Stewart, I.T., 2009. Changes in snowpack and snowmelt runoff for key mountain regions. *Hydrological Processes*, 23 (1), 78–94. doi:10.1002/hyp.7128.

Sun, C., *et al.*, 2022. CMIP6 model simulation of concurrent continental warming holes in Eurasia and North America since 1990 and their relation to the Indo-Pacific SST warming. *Global and Planetary Change*, 213, 103824. doi:10.1016/j.gloplacha.2022.103824.

Swart, N.C., *et al.*, 2019a. *CCCma CanESM5 model output prepared for CMIP6 CMIP historical*. Earth System Grid Federation. doi:10.22033/ESGF/CMIP6.3610.

Swart, N.C., *et al.*, 2019b. *CCCma CanESM5 model output prepared for CMIP6 ScenarioMIP ssp245 and ScenarioMIP ssp585*. Earth System Grid Federation. doi:10.22033/ESGF/CMIP6.1317.

Tan, M.L., *et al.*, 2020. Southeast Asia HydrO-meteorological droughT (SEA-HOT) framework: a case study in the Kelantan River Basin, Malaysia. *Atmospheric Research*, 246, 105155. doi:10.1016/j.atmosres.2020.105155.

Tatebe, H. and Watanabe, M., 2018. *MIROC MIROC6 model output prepared for CMIP6 CMIP historical*. Earth System Grid Federation. doi:10.22033/ESGF/CMIP6.5603.

Troin, M. and Caya, D., 2014. Evaluating the SWAT's snow hydrology over a Northern Quebec watershed. *Hydrological Processes*, 28 (4), 1858–1873. doi:10.1002/hyp.9730.

Tumsa, B.C., 2022. Performance assessment of six bias correction methods using observed and RCM data at upper Awash basin, Oromia, Ethiopia. *Journal of Water and Climate Change*, 13 (2), 664–683. doi:10.2166/wcc.2021.181.

Turner, S.W.D., Ng, J.Y., and Galelli, S., 2017. Examining global electricity supply vulnerability to climate change using a high-fidelity hydropower dam model. *Science of the Total Environment*, 590-591, 663–675. doi:10.1016/j.scitotenv.2017.03.022.

USGS (United States Geological Survey), 2014. *Shuttle Radar Topography Mission (SRTM): 1 arc-second global elevation database* [online]. Available from: https://earthexplorer.usgs.gov/ [Accessed 28 June 2022].

Usul, N., 2009. *Engineering hydrology*. Ankara: METU Press.

van Vliet, M.T.H., *et al.*, 2016. Power-generation system vulnerability and adaptation to changes in climate and water resources. *Nature Climate Change*, 6, 375–380. doi:10.1038/nclimate2903.

Volodin, E., *et al.*, 2019a. *INM INM-CM4-8 model output prepared for CMIP6 CMIP historical*. Earth System Grid Federation. doi:10.22033/ESGF/CMIP6.5069.

Volodin, E., *et al.*, 2019b. *INM INM-CM4-8 model output prepared for CMIP6 ScenarioMIP ssp245 and ScenarioMIP ssp585*. Earth System Grid Federation. doi:10.22033/ESGF/CMIP6.12321.

Volodin, E., *et al.*, 2019c. *INM INM-CM5-0 model output prepared for CMIP6 CMIP historical*. Earth System Grid Federation. doi:10.22033/ESGF/CMIP6.5070.

Volodin, E., *et al.*, 2019d. *INM INM-CM5-0 model output prepared for CMIP6 ScenarioMIP ssp245 and ScenarioMIP ssp585*. Earth System Grid Federation. doi:10.22033/ESGF/CMIP6.12322.

Wasti, A., *et al.*, 2022. Climate change and the hydropower sector: a global review. *Wiley Interdisciplinary Reviews: Climate Change*, 13 (2), e757. doi:10.1002/wcc.757.

Weigel, A.P., *et al.*, 2010. Risks of model weighting in multimodel climate projections. *Journal of Climate*, 23 (15), 4175–4191. doi:10.1175/2010JCLI3594.1.

Wen, K., Gao, B., and Li, M., 2021. Quantifying the impact of future climate change on runoff in the Amur River Basin using a distributed hydrological model and CMIP6 GCM projections. *Atmosphere*, 12 (12), 1560. doi:10.3390/atmos12121560.

Wieners, K.-H., *et al.*, 2019a. *MPI-M MPI-ESM1.2-LR model output prepared for CMIP6 CMIP historical*. Earth System Grid Federation. doi:10.22033/ESGF/CMIP6.6595.

Wieners, K.-H., *et al.*, 2019b. *MPI-M MPI-ESM1.2-LR model output prepared for CMIP6 ScenarioMIP ssp245 and ScenarioMIP ssp585*. Earth System Grid Federation. doi:10.22033/ESGF/CMIP6.793.

Wu, T., *et al.*, 2018. *BCC BCC-CSM2MR model output prepared for CMIP6 CMIP historical*. Earth System Grid Federation. doi:10.22033/ESGF/CMIP6.2948.

Xiang, Y., *et al.*, 2022. Impact of climate change on the hydrological regime of the Yarkant River Basin, China: an assessment using three SSP scenarios of CMIP6 GCMs. *Remote Sensing*, 14 (1), 115. doi:10.3390/rs14010115.

Xin, X., *et al.*, 2019. *BCC BCC-CSM2MR model output prepared for CMIP6 ScenarioMIP ssp245 and ScenarioMIP ssp585*. Earth System Grid Federation. doi:10.22033/ESGF/CMIP6.1732.

Yalcin, E., 2019. Estimation of irrigation return flow on monthly time resolution using SWAT model under limited data availability. *Hydrological Sciences Journal*, 64 (13), 1588–1604. doi:10.1080/02626667.2019.1662025.

Yalcin, E. and Tigrek, S., 2019. The Tigris hydropower system operations: the need for an integrated approach. *International Journal of Water Resources Development*, 35 (1), 110–125. doi:10.1080/07900627.2017.1369867.

Yukimoto, S., *et al.*, 2019a. *MRI MRI-ESM2.0 model output prepared for CMIP6 CMIP historical*. Earth System Grid Federation. doi:10.22033/ESGF/CMIP6.6842.

Yukimoto, S., *et al.*, 2019b. *MRI MRI-ESM2.0 model output prepared for CMIP6 ScenarioMIP ssp245 and ScenarioMIP ssp585*. Earth System Grid Federation. doi:10.22033/ESGF/CMIP6.638.

Ziehn, T., *et al.*, 2019a. *CSIRO ACCESS-ESM1.5 model output prepared for CMIP6 CMIP historical*. Earth System Grid Federation. doi:10.22033/ESGF/CMIP6.4272.

Ziehn, T., *et al.*, 2019b. *CSIRO ACCESS-ESM1.5 model output prepared for CMIP6 ScenarioMIP ssp245 and ScenarioMIP ssp585*. Earth System Grid Federation. doi:10.22033/ESGF/CMIP6.2291.

Zittis, G., *et al.*, 2022. Climate change and weather extremes in the Eastern Mediterranean and Middle East. *Reviews of Geophysics*, 60 (3), e2021RG000762. doi:10.1029/2021RG000762.